Cell Reports

Article

# Caveolin-1/PPARα axis suppresses T follicular helper cell response in primary Sjögren disease

## Graphical abstract

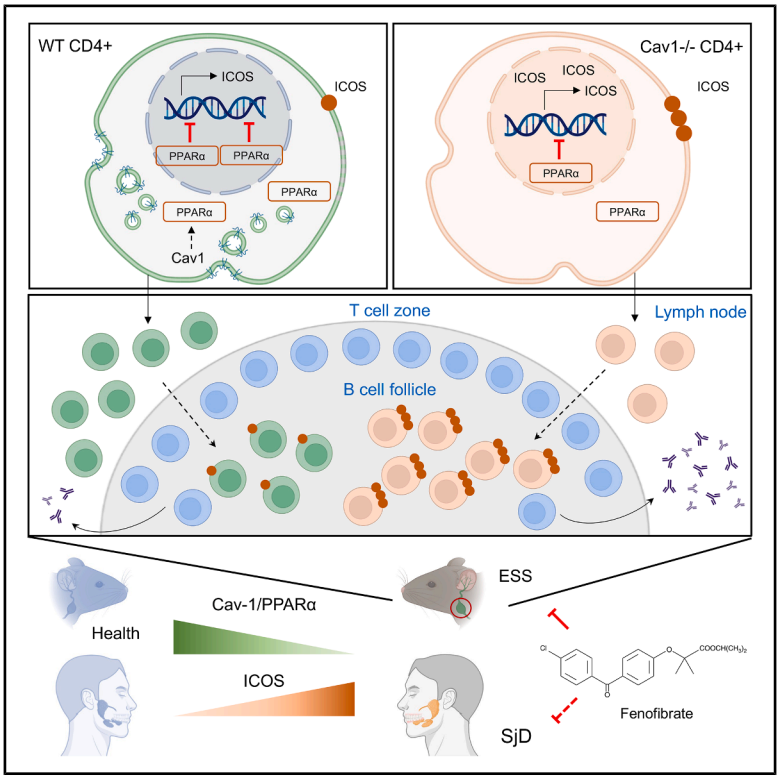


## Highlights

- Deficiency of Cav-1 exacerbates ESS development and enhanced Tfh cell response
- Cav-1 restrains ICOS-mediated Tfh cell motility toward B cell follicles
- Cav-1/PPARα axis represses *Icos* transcription in Tfh cells
- Pharmacological activation of PPARα ameliorates ESS mice with chronic inflammation

## Authors

Sulan Yu, Meiling Wu, Weizhen Zeng, ..., Yun Feng, Jiangang Shen, Xiang Lin

## Correspondence

fengyun@bjmu.edu.cn (Y.F.), shenjg@hku.hk (J.S.), linxiang@hku.hk (X.L.)

## In brief

Yu et al. show that the caveolin-1/PPARα axis represses *Icos* transcription in mouse and human pathogenic T follicular helper (Tfh) cells. Targeting this pathway with clinically available PPARα agonists such as fenofibrate has the potential to ameliorate Sjögren disease and potentially other antibody-mediated autoimmune disorders.

Yu et al., 2025, Cell Reports *44*, 116156
August 26, 2025 
https://doi.org/10.1016/j.celrep.2025.116156

CellPress

Cell Reports

CellPress
OPEN ACCESS

Article

# Caveolin-1/PPARα axis suppresses T follicular helper cell response in primary Sjögren disease

Sulan Yu,[1,7] Meiling Wu,[1,2,7] Weizhen Zeng,[3] Weiwei Fu,[4] Yacun Chen,[1] Jing Xie,[1] Philip Hei Li,[5] Yun Feng,[6,*] Jiangang Shen,[1,2,*] and Xiang Lin[1,2,8,*]

[1]School of Chinese Medicine, The University of Hong Kong, Hong Kong SAR, China
[2]State Key Laboratory of Pharmaceutical Biotechnology, The University of Hong Kong, Hong Kong SAR, China
[3]Department of Ophthalmology, Peking University Third Hospital, Beijing, China
[4]Department of Gastroenterology, Peking University Third Hospital, Beijing, China
[5]Division of Rheumatology and Clinical Immunology, Department of Medicine, Queen Mary Hospital, The University of Hong Kong, Hong Kong SAR, China
[6]Department of Ophthalmology, Peking University First Hospital, Beijing, China
[7]These authors contributed equally
[8]Lead contact
*Correspondence: fengyun@bjmu.edu.cn (Y.F.), shenjg@hku.hk (J.S.), linxiang@hku.hk (X.L.)
https://doi.org/10.1016/j.celrep.2025.116156

## SUMMARY

T follicular helper (Tfh) cells play a central role in humoral autoimmunity, including primary Sjögren disease (SjD). However, targeting Tfh cells in clinical management is challenging. Previous studies suggest that inducible T cell co-stimulator (ICOS) directs Tfh cell motility in engaging bystander B cells and promoting plasma cell differentiation. Herein, we took advantage of the mouse model of experimental Sjögren syndrome (ESS) and identified an unappreciated role of caveolin-1 (Cav-1) in suppressing ICOS expression in Tfh cells and SjD pathogenesis. Peroxisome proliferator-activated receptor alpha (PPARα), a transcription factor downstream of Cav-1, rapidly repressed *Icos* transcription upon Tfh polarization, independent of lipid metabolism. Both Cav-1 and PPARα were decreased in $CD4^+$ T cells from patients with SjD and ESS mice. Notably, the pharmaceutical agonist of PPARα suppressed human and murine Tfh cell responses both *in vitro* and *in vivo* and effectively ameliorated the disease pathology of ESS mice with chronic inflammation.

## INTRODUCTION

Primary Sjögren disease (SjD), or Sjögren syndrome, is a common autoimmune disease characterized by exocrinopathy involving the lacrimal and salivary glands (SGs), which leads to severe dry eye and dry mouth symptoms.[1] A highly activated $CD4^+$ T cell signature, including Th17 and T follicular helper (Tfh) cells, has been reported in inflamed SGs and the peripheral blood of patients with SjD.[2] We previously established a mouse model of experimental Sjögren syndrome (ESS), recapitulating the key features of human SjD.[3] Tfh cells were found to play a critical role in SjD development, as revealed by Tfh cell–deficient mice exhibiting markedly attenuated autoantibody production and disease pathology upon ESS induction.[4] Tfh cells are a subset of $CD4^+$ T cells that help B cells during germinal center (GC) reactions and promote plasma cell differentiation in adaptive immune responses.[5,6] Tfh cells are characterized phenotypically by the expression of the transcription factor B cell lymphoma 6 (Bcl-6) and the surface markers programmed cell death protein 1 (PD-1), inducible T cell co-stimulator (ICOS), and CXCR5, which mostly drive and stabilize Tfh cell positioning in B cell follicles.[7] Through the production of CD40 and cytokines (i.e., interleukin-21),[8] Tfh cells facilitate high-affinity B cell selection and antibody production. Thus, stringent Tfh cell control is critical for maintaining immune tolerance and optimal humoral responses.[6] Although the impaired regulatory function of certain immune cell subsets may contribute to hyperactive Tfh cell responses,[9] the checkpoints that maintain Tfh cell tolerance are not fully understood.

Caveolin-1 (Cav-1), a scaffold protein involved in the assembly of caveolae components and lipid domains, is structurally conserved in mammalian cells.[10] Early studies have shown that Cav-1-deficient mice remain viable but are resistant to diet-induced obesity,[11] indicating the close involvement of Cav-1 in the development of metabolic disorders. However, the role of Cav-1 in the pathogenesis of autoimmune disease remains largely unclear. Our recent studies showed that Cav-1−/− mice were resistant to experimental autoimmune encephalomyelitis (EAE), a mouse model of human multiple sclerosis.[12] Although the roles of Cav-1 in immune response are less understood, emerging studies have reported its involvement in fine-tuning T and B cell receptor signaling. Cav-1−/− B cells exhibit a reduced T cell–independent humoral immune response but a normal response to T cell–dependent antigens.[13,14] This pattern coincides with findings that Cav-1 deficiency does not affect $CD4^+$ T cell expansion following viral infection.[15] Nonetheless, it remains unknown whether and how Cav-1 regulates effector $CD4^+$ T cell subsets in SjD pathogenesis.

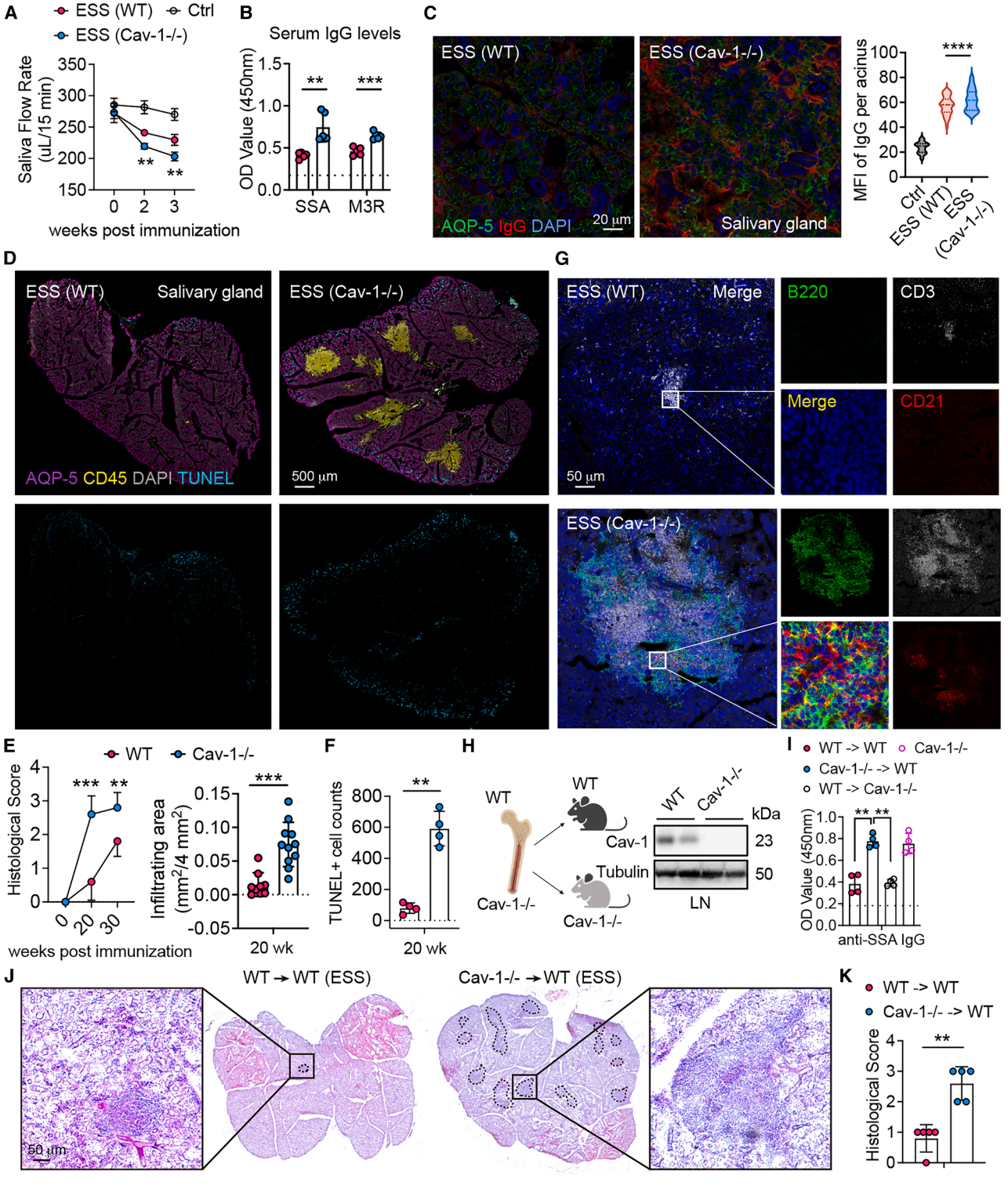


**Figure 1. Hematopoietic deficiency of Cav-1 exacerbated ESS development in mice**

(A) Salivary flow rates of WT and Cav-1−/− ESS mice were determined over time.

(B) Serum levels of autoantibodies against the SSA and M3R epitopes in WT and Cav-1−/− ESS mice 3 weeks post-immunization; dashed line indicates the levels of naive controls.

(C) Immunofluorescence staining for IgG (red) deposition on the acini (AQP-5, green) in the salivary gland of WT and Cav-1−/− ESS mice at 3 weeks post-immunization ($n$ = 80). Scale bar, 20 μm.

*(legend continued on next page)*

Here, we reported that Cav-1 deficiency does not attenuate, but rather exacerbates, ESS pathology and Tfh cell response in mice. Cav-1−/− $CD4^+$ T cells were found to express high levels of ICOS and thus exhibited increased motility toward B cell follicles. Mechanistic studies have revealed that peroxisome proliferator-activated receptor alpha (PPARα) serves as a potent transcriptional repressor of ICOS during Tfh polarization, whereas PPARα expression was found to be markedly decreased in the absence of Cav-1. Cav-1 ablation or PPARα antagonism enhanced human Tfh cell differentiation. In patients with SjD, Cav-1 levels were positively correlated with PPARα but negatively correlated with ICOS expression in circulating $CD4^+$ T cells. Fenofibrate, a US Food and Drug Administration–approved PPARα agonist, effectively suppressed both murine and human Tfh cells, which significantly ameliorated disease pathology in the established ESS mice with acute and chronic inflammation. Overall, our findings reveal an unrecognized role of the Cav-1/PPARα axis in Tfh cell dysregulation and SjD pathogenesis and that targeting PPARα may serve as a promising approach for treating Tfh cell dysregulation in patients with autoimmune diseases.

## RESULTS

### Cav-1 deficiency exacerbates ESS pathology

Although previous studies have reported ameliorated EAE pathology in Cav-1−/− mice,[12] unexpectedly, Cav-1 deficiency considerably exacerbated ESS development in mice upon disease induction, as revealed by accelerated salivary hypofunction and higher autoantibody titers than those in wild-type (WT) ESS mice (Figures 1A and 1B). This result was consistent with the enhanced deposition of IgG, a functional marker associated with dry mouth symptoms, observed on the salivary epithelium (Figure 1C).[16] Upon long-term observation, more severe tissue damage was observed in the Cav-1−/− ESS mice, along with massive lymphocytic foci and increased apoptotic epithelial cell counts, whereas age-matched WT mice exhibited only mild lymphocytic infiltration as ESS progressed (Figure 1D). Enhanced lymphocytic infiltration was also observed in the lacrimal glands (Figure S1A). Histological assessment showed that Cav-1−/− ESS mice exhibited accelerated tissue destruction and larger infiltrating areas than the WT mice during disease progression (Figures 1E and 1F). Confocal imaging analyses indicated the presence of ectopic lymphoid structures in the inflamed SG tissues of Cav-1−/− ESS mice (Figure 1G); Bcl6+$CD4^+$ T cells were observed in the B cell aggregates and T-B cell zone borders (Figures S1B and S1C). Thus, Cav-1 deficiency could promote ESS development in mice.

Given the varied abundance of Cav-1 in lymphoid and non-lymphoid organs,[17] we generated chimera mice with hematopoietic deficiency of Cav-1 for ESS induction (Figure 1H). WT recipients reconstructed with Cav-1−/− bone marrow consistently showed higher autoantibody levels (Figure 1I) and more pronounced histopathological changes (Figures 1J and 1K) than WT mice. These results suggest the importance of Cav-1 in regulating immune response during ESS development.

### Cav-1 constrains the expression of ICOS and follicular migration of Tfh cells

Previous studies, including our studies, have identified a central role of Th17 cells in both EAE and ESS pathogenesis.[3,12,18] However, phenotypic analyses have revealed that Cav-1 deficiency did not affect Th17 cell frequencies during ESS development (Figure S1D), which was consistent with previous findings in Cav-1−/− EAE mice.[12,19] In contrast, we detected significantly increased CD4+FoxP3-Bcl-6+CXCR5+ICOS+ Tfh cells in the draining cervical lymph nodes of Cav-1−/− ESS mice, whereas Treg cell counts were not affected (Figures 2A and S1E); this was associated with their follicular localization in the GCs, which may explain the expanded GC areas and increased GC B cells (Figures S1F and S1G). Thus, we sought to determine the Cav-1 levels in $CD4^+$ T cells during ESS development. A transient increase in Cav-1 expression in $CD4^+$ T cells was observed upon ESS onset, followed by persistent downregulation during disease progression (Figure 2B). Because Cav-1−/− B cells can properly respond to T cell–dependent antigens,[13] we next investigated whether Cav-1 deficiency in $CD4^+$ T cells was sufficient to cause humoral dysregulation. We first demonstrated that Cav-1 deficiency does not alter the T cell development in the thymus, in which the CD4 single-positive (SP), CD8 SP, and double-positive thymocytes were comparable between WT and Cav-1−/− mice (Figure S2A). In particular, CD24 and Qa-1,[20–22] two checkpoints in the central tolerance, were similarly expressed by the CD4 SP subpopulation (Figures S2B and S2C). These findings coincide with the peripheral tolerance at steady states in both strains (Figure S2D). WT or Cav-1−/− $CD4^+$ T cells were co-transferred with WT B cells into SG antigen–immunized immunodeficient NOD-scid-IL2Rgnull (NSG) mice. Notably, Cav-1−/− $CD4^+$ T cells markedly promoted autoreactive B cell responses (Figures 2C and S2E), resulting in elevated IgG deposition on the salivary epithelium (Figure S2F). These data suggest that Cav-1 deficiency in $CD4^+$ T cells promotes Tfh cell responses. To confirm the dominant role of Cav-1 in regulating $CD4^+$ T cell effector response in ESS development, we further validated this finding in mice deficient for Cav-1 in $CD4^+$ T cells. Consistently, Cav-$1^{fl/fl}CD4^{Cre}$

(D) Tissue damages were detected by apoptotic cells (TUNEL, cyan, bottom panel) and massive lymphocytic infiltrations (CD45, yellow) in the salivary glands (AQP-5, purple) of WT and Cav-1−/− ESS mice 20 weeks post-immunization. Scale bar, 500 μm.
(E, F) Quantification of histological score over time, while the infiltrating area and TUNEL+ cell counts were compared at 20 weeks post-immunization (each dot represented one mouse).
(G) Immunofluorescence staining of B220, CD3, and CD21 in representative focus of WT and Cav-1−/− ESS mice. Scale bar, 50 μm.
(H) Diagram of chimeric mouse model by bone marrow transfer; the genotype of the lymph nodes of recipient mice were validated upon sacrifice.
(I) Autoantibodies against the SSA epitope in the sera of chimeric ESS mice 3 weeks post-immunization; the dashed line indicates the levels of naive controls.
(J, K) Histopathological changes (J) of salivary gland of chimeric ESS mice were assessed 20 weeks post-immunization, which were scored and summarized (K); data were derived from at least three independent experiments. Data are presented as the mean ± SD; ns, not significant; $^{**}p < 0.01$; $^{****}p < 0.0001$. Scale bar, 50 μm.

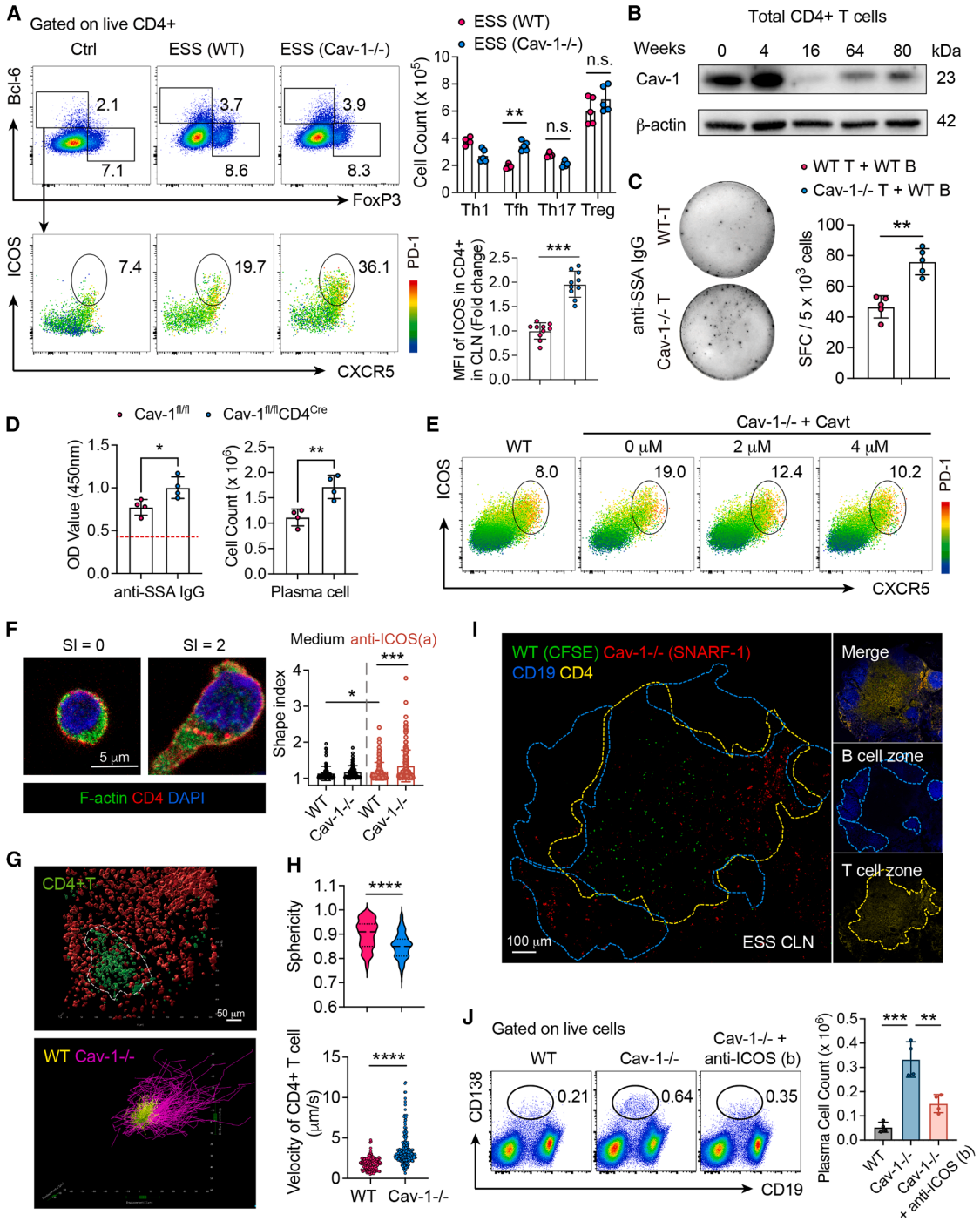


**Figure 2. Cav-1 deficiency promoted Tfh cell motility**

(A) Representative flow cytometric analysis of CD4+FoxP3-ICOS+CXCR5+PD-1+ Tfh cells in the draining cervical lymph nodes (CLN) of naive control, WT, and Cav-1−/− ESS mice, while the cell counts of Th1, Th17, Tfh, and Treg cells were summarized.

(B) Cav-1 protein levels in $CD4^+$ T cells from ESS mice were analyzed by western blot during disease progression.

(C) Immunized NSG mice were co-transferred with WT $CD19^+$ B cells and $CD4^+$ T cells from WT or Cav-1−/− mice, while enzyme-linked immunospot (ELISpot) assay was performed to determine SSA-reactive B cells in the spleen of recipient mice ($n$ = 5; mean ± SD); $^{**}p < 0.01$.

(D) Cav-$1^{fl/fl}$ and Cav-$1^{fl/fl}$ $CD4^{Cre}$ mice were immunized for ESS induction, while the serum levels of anti-SSA IgG and phenotypic analysis of splenic plasma cells were analyzed ($n$ = 4).

(E) Flow cytometric profiles of WT or Cav-1−/− $CD4^+$ T cells under Tfh polarization for 3 days, in the absence or presence of cavtratin (Cavt, $n$ = 4).

*(legend continued on next page)*

mice also exhibited higher Tfh cell frequencies in the lymphoid organs, thus displaying enhanced plasma cell differentiation and anti-Sjögren's syndrome A (SSA) IgG levels, when compared with Cav-1$^{fl/fl}$ littermates (Figures 2D, S2G). We then extended this finding in EAE, a mouse model of human multiple sclerosis.[23] Upon immunization with myelin oligodendrocyte glycoprotein (MOG), autoreactive CD4$^+$ T cells can be detected by MHC II tetramer antibodies. Although Cav-1 deficiency did not affect the MOG-reactive CD4$^+$ T cell population, consistently, MOG+CD4+T cells preferentially differentiated into Tfh cell phenotype, resulting in higher titers of anti-MOG IgG in Cav-1−/− EAE mice (Figure S2H). In cultures, Cav-1−/− CD4$^+$ T cells exhibited a higher capacity toward ICOS+CXCR5+PD-1+Tfh cell differentiation (Figures 2E and S2I). Structural biology study identified the scaffolding domain (CSD) of Cav-1 as a central docking site in signal transduction.[24] Cavtratin, a cell-permeable CSD peptide, binds caveolin-binding motifs.[25] Thus, cavtratin was found to restrain Tfh polarization from Cav-1−/− CD4$^+$ T cells, indicating the role of endogenous Cav-1 in Tfh cell differentiation. Next, we determined the featured molecules of Tfh cells, where the expression of PD-1 and ICOS, but not CXCR5, was markedly increased (Figure S2J). In addition, Cav-1−/− CD4$^+$ T cells exhibited comparable Tfh signature proteins with WT counterpart, such as CD40 ligand, Bcl-6, and representative cytokines (Figure S2K).

The ICOS-ICOS ligand (ICOSL) axis plays an indispensable role in Tfh cell motility.[26] Since WT and Cav-1−/− B cells from ESS mice exhibited similar ICOSL levels (Figure S3A), we hypothesized that increased ICOS expression in Cav-1−/−CD4$^+$ T cells might strengthen their follicular migration. We first adopted an ICOS-mediated migration assay[26] and detected pseudopod protrusion and persistent movement upon anti-ICOS-activating antibody stimulation (Figure 2F). Quantitatively, Cav-1−/− Tfh cells showed augmented pseudopod extension, which was associated with the upregulation of cytoskeleton genes related to migration (Figure S3B). Two-photon intravital imaging showed distinguishable CD4$^+$ T cell zone in the spleen post–adoptive transfer (Figure 2G). Consistently, Cav-1−/− CD4$^+$ T cells exhibited a more polarized status as reflected by lower sphericity (Figure 2H), and markedly increased motility *in situ*, as reflected by enhanced mean square displacement (Figure S3C) and velocity (Figure 2G) from cell track analysis, particularly at the T-B cell zone borders (Videos S1 and S2). This was validated by *in vitro* assays.[26] Upon ICOS ligation, Cav-1−/− Tfh cells consistently exhibited higher centroid speeds and motility (Figure S3D), thus showing enhanced migratory capacity toward CXCL13 in a transwell assay (Figure S3E). Together, these data demonstrate that Cav-1 deficiency enhances Tfh cell motility. We next determined whether Cav-1 affects follicular homing capacity of T cells under disease conditions. WT and Cav-1−/− Tfh cells from ESS mice were purified and co-transferred into WT ESS mice with active disease. As expected, Cav-1−/− Tfh cells exhibited overt follicular localization compared with their WT counterparts (Figure 2I). These data may also explain the higher ICOS+CD4$^+$ T cell frequencies in the glandular foci from Cav-1−/− ESS mice (Figure S3F).

Taken together, these results demonstrate that Cav-1 critically suppressed Tfh cell migratory capacity toward B cell follicles. Thus, we excluded this spatial factor by using co-cultures to assess the beneficial functions of B cells beyond T cell motility. Interestingly, Cav-1 deficiency did not markedly affect cognate B cell response from ESS mice, as revealed by the comparable plasmacytic differentiation and autoantibody production (Figure S4A). This result is consistent with the findings related to CD40 ligands and cytokines mentioned earlier. Thus, our data suggest that increased ICOS expression in Cav-1−/− CD4$^+$ T cells is responsible for enhanced humoral autoimmunity and ESS pathology. To validate this notion, we administered anti-ICOS-blocking antibodies to Cav-1−/− mice following ESS induction. The efficacy of the treatment was confirmed by the reduced intrafollicular ICOS+CD4$^+$ T cell counts, decreased ICOS+CXCR5+PD-1+ Tfh cell counts, and follicular homing coefficients similar to those in WT ESS mice (Figures S4B–S4D). Consequently, the reduced Tfh cell response following ICOS blockade led to decreased plasma cell counts and anti-SSA IgG levels in Cav-1−/− ESS mice (Figures 2J and S4E). These data demonstrate that Cav-1 deficiency did not affect the self-reactivity of CD4$^+$ T cells, but proportionally enhanced their pathogenicity in an ICOS-dependent manner.

## Impaired PPARα expression in CD4$^+$ T cells contributes to Cav-1-mediated Tfh cell response

Cav-1 is mainly distributed in the plasma membranes and cytoplasm, but not in the nuclei, of endothelial cells and B cells.[14,24] A similar distribution was observed in CD4$^+$ T cells (Figures S5A and S5B). Thus, we reasoned that enhanced *Icos* transcription in CD4$^+$ T cells could be indirectly regulated by Cav-1. RNA sequencing (RNA-seq) analysis suggested that PPAR signaling pathway was significantly affected by the absence of Cav-1 (Figure 3A). PPARs are a family of transcription factors, including PPARα, PPARβ/δ, and PPARγ.[27] Real-time PCR revealed that Cav-1 deficiency mainly affected the transcription of *Pparα*,

(F) Polarized states of Tfh cells purified from WT or Cav-1−/− mice, treated with isotype IgG control or anti-ICOS-activating (a) antibody ($n$ = 121–163). Scale bar, 5 μm.
(G) WT or Cav-1−/− CD4$^+$ T cells were cultured toward Tfh polarization for 3 days, followed by co-transfer with WT CD19$^+$ B cells into SG-antigen immunized NSG mice for 4 days. Two-photon intravital imaging of splenic CD4$^+$ T cells (green) and CD19$^+$ B cells (red) in the spleen of NSG mice (upper panel, Videos S1, and S2). x-y-z displacement (μm) plots of individual WT (yellow) or Cav-1−/− (magenta) CD4$^+$ T cell traces were recorded for 30 min (bottom panel). Scale bar, 50 μm.
(H) Quantitative analysis of cell tracks from (G); the starting positions overlayed and realigned at the same origin, the velocity of WT or Cav-1−/− CD4$^+$ T cells were determined, while the sphericity of each cell was summarized based on the morphology ($n$ = 152–184, only those cells that lasted at least 24 min were included; mean ± SD).
(I) CD4$^+$ T cells from WT or Cav-1−/− mice were labeled with CFSE (green) or SNARF-1 (red) respectively and co-transferred into in ESS mice with active disease for 4 days, while their distributions in the draining CLN were shown. Scale bar, 100 μm.
(J) Plasma cells in WT or Cav-1−/− ESS mice treated with vehicle or anti-ICOS blocking (b) antibodies were analyzed by flow cytometry and quantified ($n$ = 4; mean ± SD). Data are presented as the mean ± SD; ns, not significant; *$p$ < 0.05; **$p$ < 0.01; ***$p$ < 0.001; ****$p$ < 0.0001.

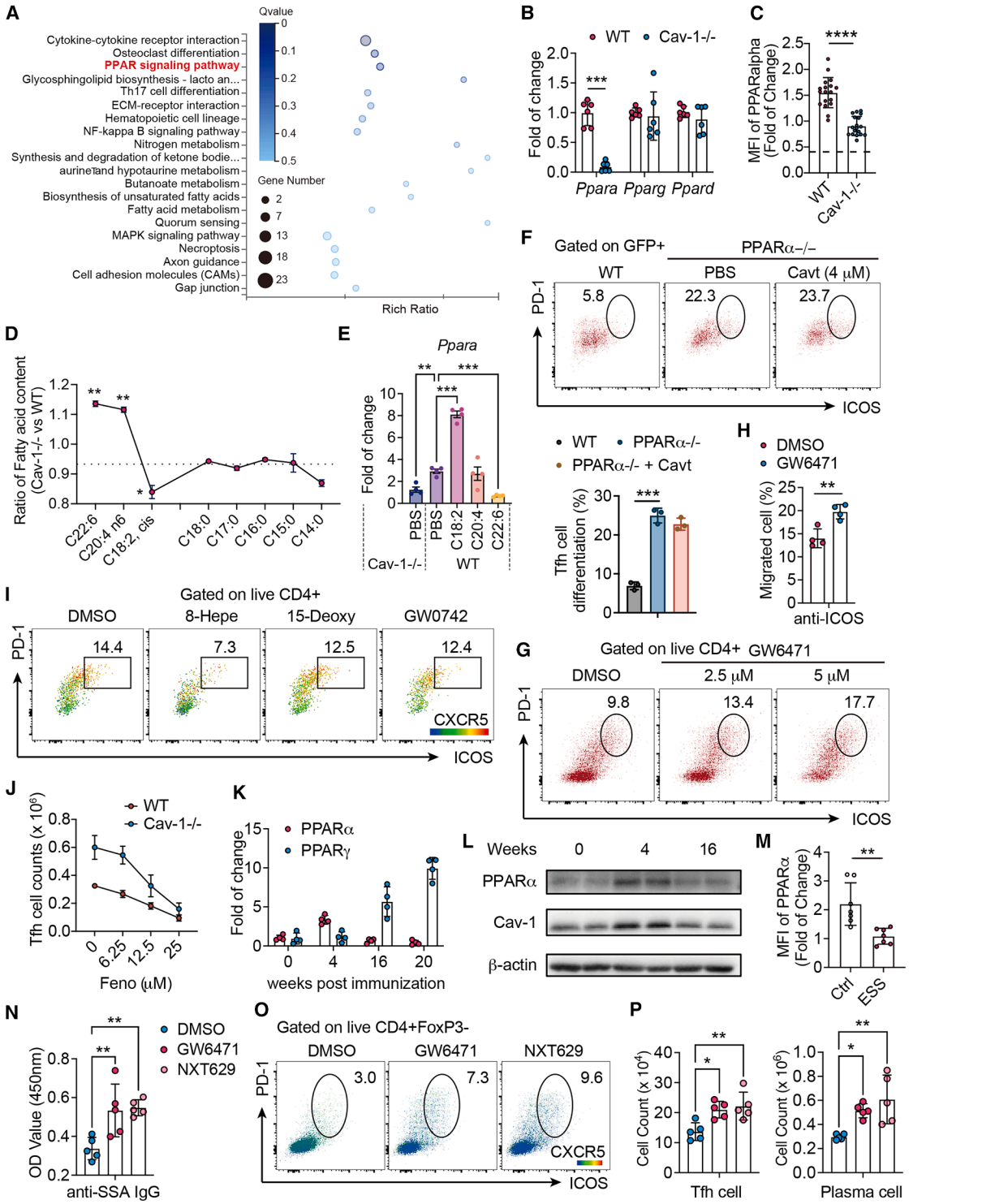


**Figure 3. Impaired PPARα expression in CD4⁺ T cells contributes to Cav-1-mediated Tfh cell response**

(A) KEGG pathway enrichment of RNA-seq analysis between WT and Cav-1−/− Tfh cells.

(B) mRNA expression of PPARα, PPARγ, and PPARδ in WT and Cav-1−/− Tfh cells.

(C) PPARα expression levels in WT and Cav-1−/− Tfh cells from ESS mice were analyzed by flow cytometry; dashed line indicates the mean fluorescence intensity (MFI) of isotype control.

*(legend continued on next page)*

whereas the expression levels of *PPARγ* and *PPARδ* were comparable to those in the WT Tfh cells (Figure 3B). Significantly reduced PPARα protein levels were also detected in the Cav-1−/− CD4$^+$ T cells (Figure 3C). Both Cav-1 and PPARα were well known to drive fatty acid metabolism.[11,28] To understand the linkage between Cav-1 deficiency and PPAR expression, we first determined the cellular fatty acids in WT and Cav-1−/− Tfh cells. Interestingly, we detected accumulated docosahexaenoic acid (DHA, C22:6(n-3)) but lower levels of linoleic acid (C18:2 (n-6)) in the absence of Cav-1 (Figure 3D). Previous studies suggested that fatty acids may modulate PPAR transcription.[29] Consistent with the outcomes reported in hepatocytes,[30] stimulation with DHA inhibited, whereas linoleic acid enhanced the expression of *Pparα*, suggesting an indirect impact upon Cav-1 deficiency in CD4$^+$ T cells (Figure 3E). To investigate whether impaired PPARα expression contributes to Tfh responses, we performed genetic ablation of PPARα in CD4$^+$ T cells using CRISPR-Cas9. Interestingly, PPARα−/−CD4$^+$ T cells also showed augmented ICOS+CXCR5+PD-1+Tfh cell differentiation, regardless of cavtratin treatment (Figure 3F), suggesting that PPARα serves as a downstream target of Cav-1 in CD4$^+$ T cells. Different from Cav-1 deficiency, PD-1 expression was comparable between WT and PPARα$^{-/-}$ Tfh cells (Figure S5C), indicating that PD-1 may be affected by Cav-1 in a PPARα-independent manner. This effect could be achieved by treatment with GW6471, a selective PPARα antagonist toward Tfh differentiation (Figure 3G), and in the ICOS-mediated transwell assay (Figure 3H). Previous studies discovered 8-hydroxyeicosapentaenoic acid (8-HEPE), 15-deoxy-D12,14-prostaglandin J2 (15-Deoxy), and GW0742,[31] as the selective agonist against PPARα, PPARβ/δ, and PPARγ, respectively. In contrast, only PPARα agonist treatment effectively suppressed Tfh cell differentiation (Figure 3I). To avoid potential off-target effects, we used fenofibrate, a pharmaceutical agonist of both human and murine PPARα for validation,[28] which dose-dependently suppressed both WT and Cav-1−/− Tfh differentiation in culture (Figure 3J). These data suggest that PPARα is responsible for Cav-1 signaling and serves as a negative regulator of Tfh cell differentiation. During ESS development, similar to Cav-1 expression in CD4$^+$ T cells, we also observed a transient increase of PPARα, but progressively decreased during disease progression, which was not seen in PPARγ (Figures 3K–3M, S5D, S5, and S5E). As expected, treatment with two selective PPARα antagonists, GW6471 and NXT629, enhanced Tfh cell responses and thus resulted in higher plasma cell count serum titers of anti-SSA IgG in ESS mice (Figures 3N–3P). Together, these results demonstrate the functional importance of the Cav-1/PPARα axis in restraining Tfh cells.

## PPARα represses *Icos* transcription in Tfh cells

Previous studies suggest the downregulation of lipid metabolic processes as a major consequence of Cav-1 deficiency, with PPARα being responsible.[32] Indeed, less lipid droplets were observed in Cav-1-deficient CD4$^+$ T cells (Figure 4A), particularly in the effector population (Figure S6A). Thus, we investigated whether lipid metabolism is involved in Cav-1/PPARα axis-mediated ICOS expression in Tfh cells. We first monitored the transcriptional regulation of *Icos* during Tfh polarization, which was significantly increased as early as 16 h in Cav-1−/− CD4$^+$ T cells, followed by elevated proteins upon Tfh differentiation (Figure 4B). Because lipid metabolism–mediated energy generation consists of several rate-limiting steps,[33] in which fatty acid β-oxidation (FAO) produces acetyl coenzyme A (CoA) that enters the mitochondrial tricarboxylic acid cycle, we next determined whether *Icos* transcription was altered during this process. We measured mitochondrial respiration in fatty acids using palmitic acid (16:0) as the sole extracellular substrate.[34] Cav-1 deficiency markedly decreased the basal and maximal respiratory capacity 48 h post-Tfh polarization (Figures 4C and S6B). Accordingly, the protein levels of acyl-CoA dehydrogenase medium chain, the representative enzyme of FAO initiation, were decreased in the absence of Cav-1. Likewise, succinyl-CoA synthetase and aconitase, key regulatory enzymes in the tricarboxylic acid cycle, were also reduced in Cav-1−/− CD4$^+$ T cells 48 h post-stimulation (Figure 4D). This was associated with a decreased cellular fatty acid content (Figure 4E). However, these effects were not observed at the early stages of Tfh polarization. FAO and the cellular fatty acid levels were minimal or undetectable

(D) CD4$^+$ T cells from WT and Cav-1−/− ESS mice were cultured toward Tfh polarization for 3 days. The ratio of different fatty acids was determined by gas chromatography-mass spectrometry.
(E) WT or Cav-1−/− CD4+T cells were cultured toward Tfh differentiation, while WT Tfh cells were treated with C18:2, C20:4, or C22:6 fatty acids or vehicle. mRNA expression of PPARα was analyzed after 3 days ($n$ = 4).
(F) Purified CD4$^+$ T cells from WT mice were transduced with GFP-incorporated plasmids for PPARα deletion, followed by Tfh polarization for 3 days, while GFP+PD-1+ICOS+CXCR5+ Tfh cell differentiation was analyzed by flow cytometry.
(G) CD4$^+$ T cells were purified and polarized into Tfh cells in the absence or presence of GW6471 for 3 days while the phenotypic analysis was performed.
(H) CD4$^+$ T cells from (E) were pre-treated with anti-ICOS-activating antibody and subjected to transwell assay toward recombinant CXCL13 in the bottom chamber.
(I) Flow cytometric profiles of Tfh cells in the absence or presence of 8-Hepe, 15-Deoxy, or GW0742.
(J) WT or Cav-1−/− CD4+T cells were cultured toward Tfh differentiation in the presence of fenofibrate (Feno) at various concentrations, while Tfh cell counts were analyzed by flow cytometry.
(K) mRNA expression of PPARα and PPARγ in CD4$^+$ T was analyzed at different time points during ESS development.
(L) Cav-1 and PPARα protein levels in the CD4$^+$ T cells were analyzed by western blot at different time points during ESS development.
(M) PPARα expression levels in CD4$^+$ T cells from naive and ESS mice were analyzed by flow cytometry.
(N) Mice were immunized for ESS induction and treated with vehicle, GW6471, or NXT629, while the serum levels of autoantibodies against the SSA epitopes were analyzed ($n$ = 5).
(O) Mice were immunized for ESS induction and treated with vehicle, GW6471, or NXT629, while the Tfh cells were analyzed by flow cytometry.
(P) ESS mice were treated with vehicle, GW6471, or NXT629 for 3 weeks, while the cell counts of Tfh cells (left) and plasma cells (right) were analyzed by flow cytometry. Data are presented as the mean ± SD; *$p$ < 0.05; **$p$ < 0.01; ***$p$ < 0.001.

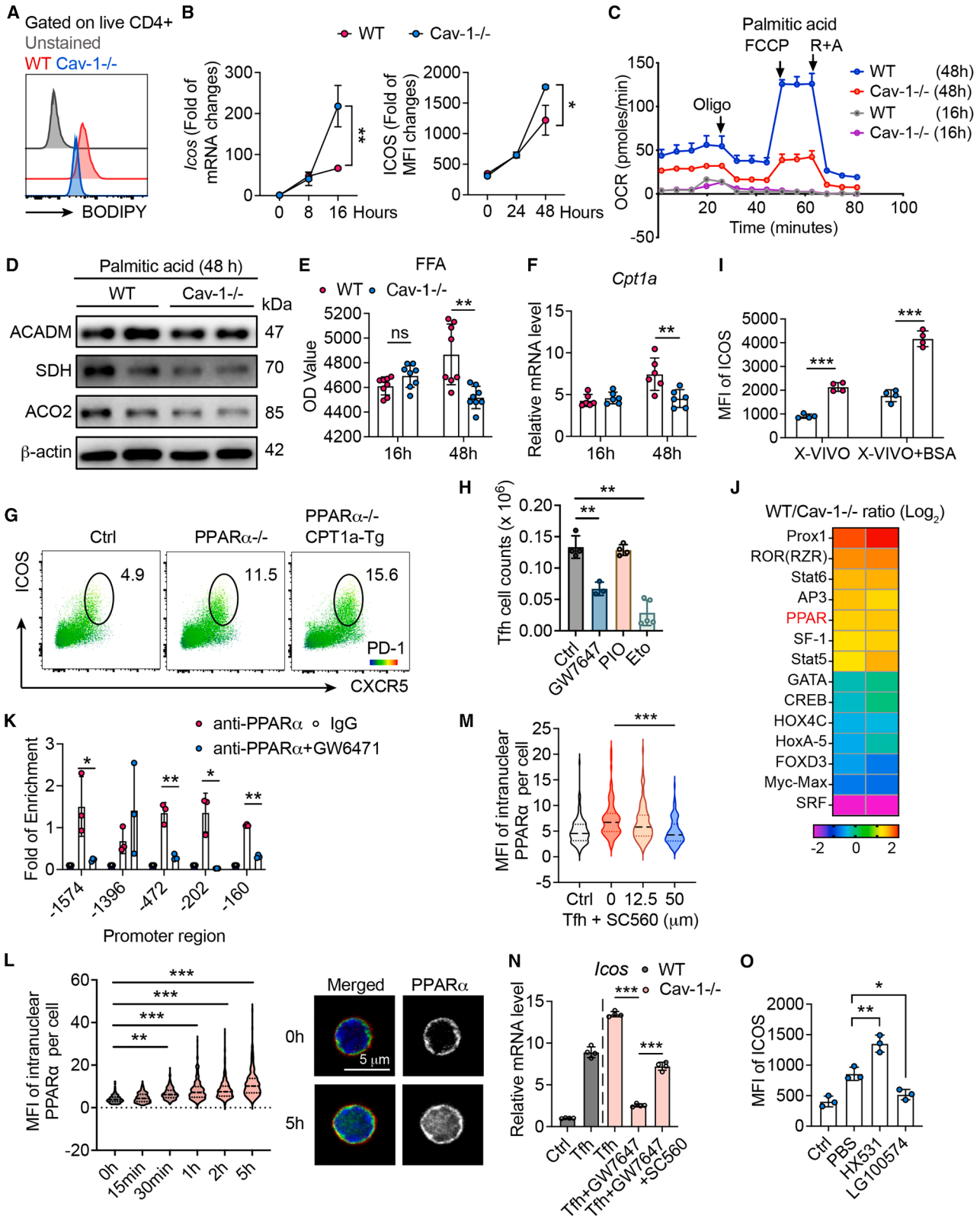


(legend on next page)

in both WT and Cav-1−/− $CD4^+$ T cells 16 h post-stimulation, whereas there was no significant difference in the enzyme expression levels. Taken together, these results confirm that Cav-1 deficiency impairs FAO. However, the rapid increase in *Icos* transcription in Cav-1−/− $CD4^+$ T cells before the energy status transition suggests that transcriptional regulation occurred in a relatively direct manner.

To validate this notion, we next investigated the target gene of PPARα in $CD4^+$ T cells. *Cpt1a* is a highly conserved PPARα-targeted gene and metabolic regulator in FAO process through the carnitine palmitoyltransferase (CPT) system.[35] Consistently, *Cpt1a* expression was lower in the Cav-1−/− T cells 48 h post-Tfh differentiation compared with WT controls, but not in the early phase of Tfh polarization (Figure 4F). Next, we overexpressed *Cpt1a* in $CD4^+$ T cells to restore, at least partially, PPARα deficiency-mediated lipid metabolism. Surprisingly, *Cpt1a* overexpression did not suppress but rather promoted ICOS expression in PPARα$^{-/-}$ Tfh cells (Figure 4G), whereas irreversible CPT1A antagonism by etomoxir limited ICOS expression (Figure 4H). This can be attributed to the globally intervened energy generation and requirements. This notion was further supported by establishing fatty acid–free culture conditions, in which Cav-1−/− $CD4^+$ T cells retained a higher capacity for ICOS expression (Figures 4I and S6C). In this context, the addition of nutrients through bovine serum albumin further enhanced Tfh cell differentiation in both WT and Cav-1−/− $CD4^+$ T cells. These results demonstrate that impaired lipid metabolism in Cav-1−/− $CD4^+$ T cells does not attribute to the increased *Icos* transcription.

PPARα also limits inflammatory responses through transcriptional repression,[27] via a conserved mechanism in forming heterodimers with 9-*cis*-retinoic acid receptor (RXR), and then binds the peroxisome proliferator response element at the promoter region of the target genes.[36] Transcriptomic screening revealed the lower binding activity of PPARα in Cav-1−/− $CD4^+$ T cells (Figure 4J). Consequently, chromatin immunoprecipitation (ChIP)-PCR analysis indicated that PPARα rapidly bound to the *Icos* promoter region 16h post-Tfh polarization, but largely abrogated by PPARα antagonism (Figure 4K). This finding was further supported by interfering with intranuclear translocation. Time-series imaging showed that the intranuclear translocation of PPARα began at 30 min and persisted for hours (Figure 4L). Early studies have suggested a role for COX-1 inhibitor in the nuclear translocation of PPARs.[37,38] We validated this finding in $CD4^+$ T cells by using SC-560, a selective COX-1 inhibitor (Figure 4M), which abolished PPARα agonist-mediated *Icos* transrepression (Figure 4N). Similarly, the capacity of RXR binding to the *Icos* promoter could be enhanced by a PPARα agonist but inhibited by an antagonist (Figure S6D). Thus, the selective RXR antagonist HX531 and the RXR agonist LG100754,[39] respectively, enhanced and inhibited ICOS expression *in vitro* (Figures 4O and S6E). Collectively, these data demonstrate that PPARα acts as a repressor of *Icos* transcription.

## The Cav-1/PPARα axis critically regulates human Tfh cells

We next investigated whether the Cav-1/PPARα axis also operates in human T cells. Purified $CD4^+$ T cells from healthy donors were transduced with GFP-incorporated plasmids for Cav-1 deletion. Similar to the murine system, Cav-1−/−hCD4+ T cells exhibited a strong capacity for ICOS+CXCR5+PD-1+ Tfh differentiation with increased ICOS and PD-1 expression (Figures 5A, 5B, and S7A), whereas their PPARα expression was significantly decreased (Figure 5C). We then determined the suppressive effects of fenofibrate on Tfh cell differentiation, which yielded a half-maximal inhibitory concentration ($IC_{50}$)

**Figure 4. PPARα represses ICOS transcription in Tfh cells**

(A) Lipid droplet staining by BODIPY in $CD4^+$ T cells from WT or Cav-1−/− ESS mice.

(B) mRNA (left panel) and protein (right panel) levels of ICOS from Tfh cells at different time points.

(C) $CD4^+$ T cells from WT or Cav-1−/− mice were cultured under Tfh polarization conditions, while mitochondrial oxygen consumption rate (OCR) levels at 16 and 48 h were determined with palmitic acid as the sole substrate.

(D) Protein expressions of ACADM, SDH, ACO2, and β-actin in WT and Cav-1−/− $CD4^+$ T cells 48 h post-Tfh polarization were analyzed by western blot.

(E, F) Free fatty acid content and mRNA expression of *Cpt1a* in the WT or Cav-1−/− $CD4^+$ T cells at 16 and 48 h post-Tfh polarization were analyzed by ELISA ($n$ = 8) and qPCR ($n$ = 6), respectively.

(G) WT and PPARα$^{-/-}$ $CD4^+$ T cells with or without *Cpt1a* gene overexpression (Tg) were cultured under Tfh polarization for 3 days, while PD1+ ICOS+ phenotype was analyzed by flow cytometry.

(H) $CD4^+$ T cells from WT mice were cultured under Tfh polarization conditions, in the absence or presence of GW7647, pioglitazone (PIO), or etomoxir (Eto) for 3 days, while Tfh cells were analyzed by flow cytometry and enumerated.

(I) $CD4^+$ T cells from WT or Cav-1−/− mice were cultured with fatty acid free medium X-VIVO toward Tfh differentiation, in the absence or presence of bovine serum albumin (BSA) for 3 days, while ICOS expression was analyzed by flow cytometry.

(J) $CD4^+$ T cells from WT mice were cultured under Tfh polarization conditions for 16 h, while the binding activities of various transcription factors were assessed. The 14 mostly differentially active transcription factors were listed in the heatmap.

(K) $CD4^+$ T cells from WT mice were cultured under Tfh polarization conditions for 16 h, while anti-PPARα ChIP-PCR assay was performed to reveal the binding sites in the *Icos* promoter.

(L) $CD4^+$ T cells (red) from WT mice were cultured under Tfh polarization conditions, while nuclear expression of PPARα (green) was determined by confocal microscopy at different time points ($n$ = 368–443). Scale bar, 5 μm.

(M) $CD4^+$ T cells from WT mice were cultured under Tfh polarization conditions for 5 h, in the absence or presence of SC560, while nuclear translocation of PPARα was quantified by confocal microscopy ($n$ = 30).

(N) $CD4^+$ T cells from WT or Cav-1−/− mice were cultured under Tfh polarization conditions for 16 h, in the absence or presence of GW7647 and SC560, while *Icos* expression levels were determined by qPCR.

(O) $CD4^+$ T cells from WT mice were cultured under Tfh polarization conditions for 3 days, in the absence or presence of HX531 or LG100574, while ICOS expression was determined by flow cytometry; data were derived from at least three independent experiments. Data are presented as the mean ± SD; $^*p < 0.05$; $^{**}p < 0.01$; $^{***}p < 0.001$.

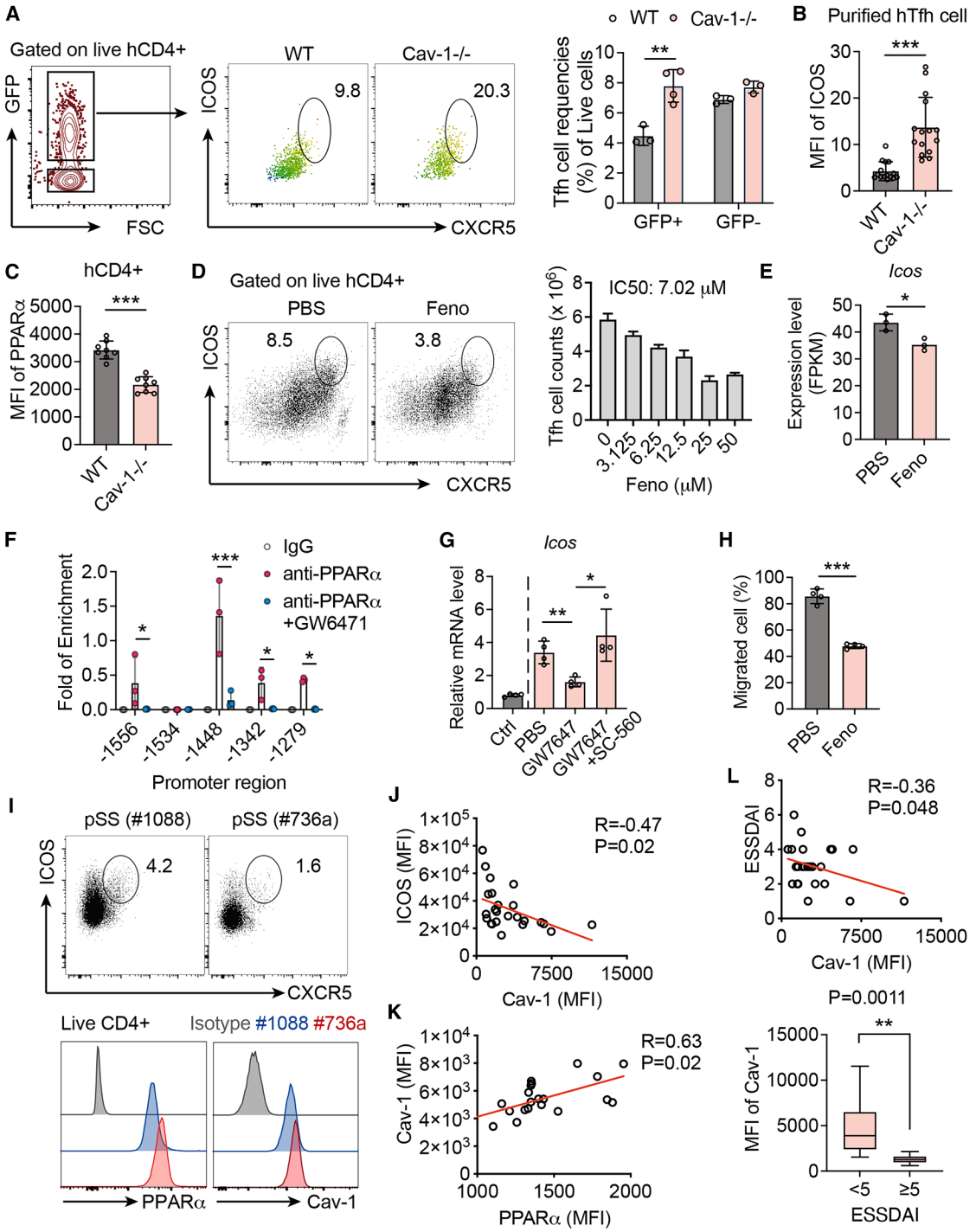


**Figure 5. Cav-1/PPARα axis critically regulates human Tfh cells**

(A) Purified CD4$^+$ T cells from healthy donors were transduced with GFP-incorporated plasmids for Cav-1 deletion, followed by Tfh polarization for 3 days, while Tfh cell differentiation was analyzed by flow cytometry.

(B, C) Upon Tfh polarization for 3 days, protein levels of ICOS ($n$ = 15) and PPARα ($n$ = 8) in CD4$^+$ T cells were determined by flow cytometry.

(D) Purified CD4+T cells from healthy donors were cultured toward Tfh differentiation for 3 days in the presence of Feno at various concentrations, while Tfh cell counts were analyzed by flow cytometry.

(E) Purified CD4+T cells from healthy donors were cultured toward Tfh differentiation for 16 h and paired-end RNA-seq analyzed was performed. The transcription reads, revealed by FPKM of *Icos* gene, were shown.

(F) Under culture condition described in (E), anti-PPARα ChIP-PCR assay was performed to reveal the binding sites in the *Icos* promoter.

*(legend continued on next page)*

of 7.024 μM (Figures 5D and S7B). RNA-seq analysis showed that fenofibrate significantly suppressed the *Icos* transcript copies 16 h post-Tfh polarization (Figure 5E), strongly supporting our findings in mice. Consistently, human PPARα also rapidly bound to the *Icos* promoter region during Tfh polarization, as revealed by ChIP-PCR analysis, which can be abolished by PPARα antagonism and blockage of intranuclear entry (Figures 5F and 5G). Functional assay further verified that ICOS-mediated migration is inhibited by fenofibrate (Figure 5H). To validate this phenotype under disease conditions, we analyzed circulating $CD4^+$ T cells in patients with SjD, showing a strong positive correlation between PPARα and Cav-1 (Figure 5I). Interestingly, patients with higher frequencies of ICOS+CXCR5+PD-1+ Tfh (cTfh) cells exhibited relatively lower levels of Cav-1 and PPARα in $CD4^+$ T cells, resulting in a negative correlation between Cav-1 and ICOS expression (Figures 5J and 5K). Similar to the findings in ESS mice, Cav-1 levels in $CD4^+$ T cells were negatively correlated with disease activity in patients with SjD (Figure 5L). These results demonstrate that the Cav-1/PPARα axis acts as a negative regulator in human Tfh cells, whereas targeting PPARα may represent a promising approach for treating Tfh cell dysregulation.

### Pharmaceutical activation of PPARα ameliorates ESS development

Fenofibrate has a similar affinity and high efficacy for both murine and human PPARα[28] and thus yielded an $IC_{50}$ of 8.39 μM against murine Tfh cells (Figure S8A). This prompted us to explore the therapeutic potential of pharmaceutical PPARα agonism in ESS. Thus, ESS mice with acute inflammation meeting the SjD diagnostic criteria (i.e., reduced saliva secretion and elevated autoantibody levels) were treated with either fenofibrate or vehicle (Figure 6A). The dosage was translated from the human doses used in clinical trials[40,41] such as primary biliary cirrhosis, a chronic autoimmune disease commonly associated with SS.[42] Methotrexate (MTX), one of the first-line medications, served as control treatment.[43] Both fenofibrate and MTX effectively ameliorated salivary hypofunction and decreased the serum anti-SSA IgG levels (Figures 6B and 6C). Phenotypic analyses further showed that fenofibrate treatment significantly suppressed Tfh cell responses, particularly the GC Tfh cell counts (Figures 6D and S8B). This was also associated with reductions in the GC area, GC B cell, and plasma cell counts (Figures 6D and S8C). Although MTX treatment restrained B cell response, it did not affect Tfh cell counts in ESS mice. This was consistent with the recent clinical findings that MTX mainly targeted B cell compartment but did not restrain, rather increased, circulating Tfh cells in patients.[44] We next assessed the therapeutic potential of fenofibrate against chronic inflammation. ESS mice immunized for 20 weeks at acute-chronic disease stages, as indicated by moderate lymphocytic infiltration in the SG (Figure S8D), were treated with fenofibrate for 10 weeks (Figure 6A). Histopathological findings showed significantly reduced tissue damage and inflammation in the SG of fenofibrate-treated ESS mice, as evidenced by diminished lymphocytic infiltration and fewer apoptotic epithelial cells (Figures 6E–6G). Consequently, no obvious ectopic lymphoid structures were detected in the SG of fenofibrate-treated ESS mice (Figure S8E). However, the disease outcome in ESS mice with MTX treatment was not improved at chronic stages. Consistently, fenofibrate, but not MTX, markedly decreased FoxP3-Bcl-6+ICOS+CXCR5+PD-1+ Tfh cells, GC B cells, and plasma cells in ESS mice with chronic inflammation (Figures 6H–6J, S8F, and S8G). A recent study reported a humanized mouse model in which NSG mice were transplanted with peripheral blood mononuclear cells (PBMCs).[45] Thus, we adopted this method by dividing PBMCs from each patient with SjD into two groups for paired analysis, followed by PBS or fenofibrate treatment. Importantly, Tfh cells derived from patients were effectively suppressed by fenofibrate (Figure 6K). Consistent with the findings from cell culture, fenofibrate did not affect PD-1 expression in $CD4^+$ T cells in recipient mice (Figure S8H). Collectively, these results provide strong evidence that targeting PPARα could be a promising therapeutic approach for SjD and autoimmune disorders associated with dysregulated Tfh cell responses.

## DISCUSSION

Tfh cells play a central role in the pathogenesis of humoral autoimmune diseases. However, the mechanism underlying Tfh cell-intrinsic tolerance is not fully understood. In this study, to the best of our knowledge, we demonstrated that the Cav-1/PPARα axis negatively regulates the Tfh cell migration capacity, with PPARα rapidly binding to the promoter region of *Icos* upon Tfh polarization. This finding was further supported by observations in Cav-1-deleted and PPARα-activated human $CD4^+$ T cells. In the context of autoimmunity, a negative correlation between Cav-1 and ICOS in $CD4^+$ T cells was observed in patients with SjD, whereas pharmaceutical activation of PPARα effectively ameliorated the pathology of ESS in both acute and chronic stages.

(G) Purified CD4+T cells from healthy donors were cultured toward Tfh differentiation for 16 h, in the absence or presence of GW7647 and SC560, while *Icos* expression levels were determined by qPCR.
(H) Purified CD4+T cells from healthy donors were cultured toward Tfh differentiation for 3 days, in the absence or presence of Feno treatment, while T cells were subjected to transwell assay toward recombinant CXCL13 in the bottom chamber.
(I) Correlation between Cav-1 and PPARα expression levels in the $CD4^+$ T cells in the peripheral blood of SjD patients was analyzed by Pearson's correlation coefficient ($n = 24$).
(J) Representative flow cytometric analysis of circulating Tfh cells from SjD patients, while the expression levels of Cav-1 and ICOS were determined.
(K) Correlation between Cav-1 and PPARα expression levels in the $CD4^+$ T cells in the peripheral blood of SjD patients was analyzed by Pearson's correlation coefficient.
(L) Correlation between Cav-1 expression levels in the circulating $CD4^+$ T cells and disease activities (ESSDAI) of SjD patients was analyzed by Pearson's correlation coefficient ($n = 24$). Data were derived from at least three independent experiments. Data are presented as the mean ± SD; $^*p < 0.05$; $^{**}p < 0.01$; $^{***}p < 0.001$.

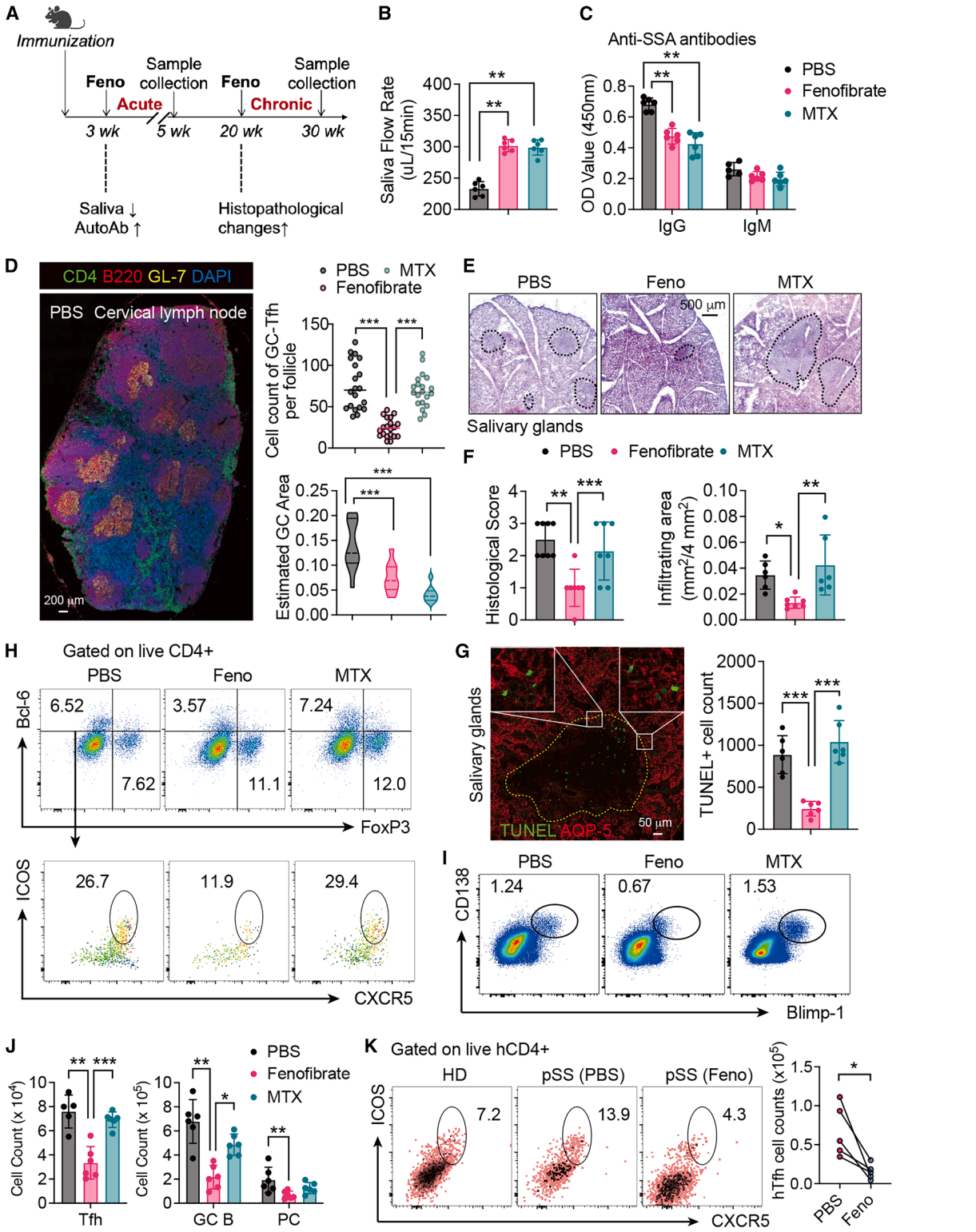


**Figure 6. Pharmaceutical activation of PPARα ameliorated ESS development**

(A) Diagram of Feno intervention strategies on ESS mice at acute or chronic stages.

(B, C) At acute stages, ESS mice were treated with PBS vehicles, Feno (40 mg/kg), or methotrexate (MTX, 1 mg/kg), while salivary function and serum levels of anti-SSA IgG antibodies were assessed.

*(legend continued on next page)*

Currently, there are limited investigations into how Cav-1 modulates Th cell responses. Recent studies, including our own, have reported comparable Th1 and Th17 cell counts between WT and Cav-1−/− mice with active EAE.[12,19] The pathological remission of EAE was mainly attributed to altered tight junction remodeling in the blood-brain barrier, leading to decreased infiltrations in the spinal cord. Notably, early studies have demonstrated that the transfer of myelin-specific Tfh cells did not induce EAE development,[46] which may explain the differential outcomes between EAE and ESS mice with Cav-1 deficiency.

Several studies have highlighted alterations in PPAR and FAO pathways from Gene Ontology in immune cells (e.g., macrophages[47]) and tissue cells (e.g., hepatocytes[32]). Fatty acid has been recently reported to be involved in immune homeostasis, in which proper lipid metabolism, e.g., peroxidation by glutathione peroxidase 4 (Gpx4), modulates Tfh cell maintenance.[48] In the absence of Cav-1, we detected impaired FAO cascade activity, including Gpx4, and reduced PPARα in $CD4^+$ T cells. However, lipid metabolism is a rate-limiting process during long-term T cell differentiation and does not account for the rapid *Icos* transcription observed in Cav-1−/−$CD4^+$ T cells at the Tfh initiation stage. Another pivotal function of PPARs is the inhibition of inflammatory gene expression, in which PPARγ has been extensively studied.[49] In this study, we demonstrated that PPARα binds to and represses the *Icos* promoter. Taken together, our results suggest that the Cav-1/PPARα axis acts as a checkpoint in Tfh cell tolerance, rather than merely serving as a metabolic regulator.

Although altered Cav-1 expression levels have been reported in various diseases, investigations into the role of Cav-1 in autoimmune pathogenesis are few. Reduced Cav-1 expression has been observed in the skin tissue of patients with systemic sclerosis.[50] Recent findings suggest that lower bile acid levels in Cav-1−/− mice may account for the insufficient activation of FXRα, a critical regulator of PPARα in hepatocytes.[32] This finding coincides with the comorbidity of liver involvement in SjD, as biliary cirrhosis is commonly observed in patients with SjD, along with reduced bile acid levels.[51] In contrast to Cav-1, emerging evidence highlights the role of PPARs in autoimmune disorders. PPARα agonists have been reported to interfere with proinflammatory cytokines produced by various cell types, demonstrating beneficial effects in mouse models of autoimmune thyroid diseases, multiple sclerosis, and systemic lupus erythematosus.[52] PPARα is well conserved between humans and mice, and pharmaceutical agonists can selectively activate both human and murine PPARα,[28] potentiating the clinical application of drug screening in mouse models.[52] Fenofibrate has been clinically prescribed for decades, showing good tolerance and safety for long-term human use.[53] Given that fenofibrate is already used in patients with biliary cirrhosis, our findings may support its use in patients with SjD. Herein, we demonstrated that fenofibrate effectively ameliorated ESS in mice, particularly under chronic inflammatory conditions. Overall, our results suggest that targeting Cav-1 or PPARα could be a promising strategy for treating autoimmune disorders accompanied by Tfh cell dysregulation, and the expression levels of Cav-1 or PPARα may be considered factors for patient stratification and cohort selection.

## Limitations of the study

Although our present study has proposed a future approach of targeting PPARα in SjD, first-line medications are still essential for patients diagnosed with SjD. However, there is a lack of evidence-based studies using combined therapy of fenofibrate and disease-modifying antirheumatic drugs in patients with rheumatic diseases. Thus, safety and efficacy are both required to be tested, e.g., in humanized mouse model,[54] and further verified in the clinical trial of fenofibrate treatment in SjD. Furthermore, it is not clear whether patient cohorts with normal PPARα expression levels would have different response to fenofibrate, highlighting the need for biomarker-driven patient stratification.[55] Additionally, the broader immunomodulatory effects of PPARα activation on non-Tfh immune cell populations (e.g., B cells, macrophages) warrant further investigation to fully understand its clinical applicability.

## RESOURCE AVAILABILITY

### Lead contact

Requests for further information and resources should be directed to and will be fulfilled by the lead contact, Xiang Lin (linxiang@hku.hk).

### Materials availability

This study did not generate new unique reagents.

### Data and code availability

- The assigned accession of the RNA sequencing data is HRA005595. Please access it from the following link: https://bigd.big.ac.cn/gsa-human/browse/HRA005595. All data are publicly available as of the date of publication. Original western blot images and microscopy data reported in this paper will be shared by the lead contact upon request.
- All data are included in this manuscript and are available from the lead contact upon reasonable request.
- Any additional information required to reanalyze the data reported in this paper is available from the lead contact upon request.

(D) At acute stages, GCs in the draining lymph nodes from ESS mice were marked by GL-7 (yellow), while the GC area and GC-Tfh cell counts per follicle were determined ($n$ = 20). Scale bar, 200 μm.

(E–G) At chronic stages, ESS mice (20 weeks post-immunization) were treated with PBS vehicles, Feno, or MTX for 10 weeks as illustrated in (A), and the histopathological changes in SG were shown by H&E staining (E); scale bar, 500 μm. The infiltrating area and histological score were further quantified (F), while the glandular damages, as characterized by lymphocytic infiltration (magenta) and TUNEL (green) staining, were assessed by confocal microscopy (G); scale bar, 50 μm.

(H–J) At chronic stages, phenotypic analysis of Tfh cells in the draining lymph nodes (H) and splenic plasma cells (I) of ESS mice with interventions were performed by flow cytometry, while the cell counts were summarized (J).

(K) PBMCs of healthy donor (HD) or SjD patients were adoptively transferred into NSG mice, among which equal amount of PBMCs from each SjD patient was transferred into paired NSG mice, followed by PBS or Feno treatment for 1 week. Tfh cells in the spleen were analyzed by flow cytometry and enumerated; data were derived from at least three independent experiments. Data are presented as the mean ± SD; $^*p < 0.05$; $^{**}p < 0.01$; $^{***}p < 0.001$.

## ACKNOWLEDGMENTS

This work was funded by grants through National Key Research and Development Program of China (2023YFE0203100), Mainland-Hong Kong Joint Funding Scheme (MHP/104/22), General Research Fund, Hong Kong Research Grants Council (17116521, 27111820, and 17109123), Health and Medical Research Fund (19201121 and 20212601), and Hong Kong Research Grants Council Area of Excellence Scheme 2016/2017 (no. AoE/P-705/16). We thank the staff of Faculty Core Facility, Li Ka Shing Faculty of Medicine, The University of Hong Kong, for their kind support.

## AUTHOR CONTRIBUTIONS

Conceptualization, X.L. and J.S.; methodology, X.L., S.Y., M.W., W.Z., W.F., Y.F., and J.S.; investigation, S.Y., M.W., W.Z., W.F., Y.C., J.X., P.H.L., and X.L.; original draft, X.L., S.Y., and M.W.; writing – review and editing, X.L., J.S., and Y.F.; funding acquisition, X.L., J.S., and Y.F.; resources, X.L., J.S., Y.F., and P.H.L.; supervision, X.L., J.S., and Y.F.

## DECLARATION OF INTERESTS

The authors declare no competing interests.

## STAR★METHODS

Detailed methods are provided in the online version of this paper and include the following:

- KEY RESOURCES TABLE
- EXPERIMENTAL MODEL AND STUDY PARTICIPANT DETAILS
  - Human samples and ethics
  - Mice and ethics
  - ESS induction in mice
  - Primary murine naive $CD4^+$ T cell culture
  - Primary human naive $CD4^+$ T cell culture
- METHOD DETAILS
  - Construction of bone marrow chimaeras
  - Human cell collection
  - Saliva and blood collection
  - Histological assessment
  - Immunofluorescence microscopy
  - Two-photon live imaging of T/B cells motility *in vivo*
  - Transwell migration assay
  - Imaging of T cell actin cytoskeleton *in vitro*
  - Imaging of T cell motility *in vitro*
  - Flow cytometry
  - Western blot analysis
  - ELISA
  - ELISpot assay
  - RT-qPCR and RNA-seq analysis
  - Chromatin immunoprecipitation (ChIP)-qPCR
  - Seahorse assay
  - Transcription factor (TF) binding profiling
- QUANTIFICATION AND STATISTICAL ANALYSIS
  - Polarized states of Tfh cells
  - Quantification of cell migration
  - Statistical analysis

## SUPPLEMENTAL INFORMATION

Supplemental information can be found online at https://doi.org/10.1016/j.celrep.2025.116156.

Received: November 25, 2024
Revised: May 27, 2025
Accepted: July 25, 2025
Published: August 12, 2025

## REFERENCES

1. Nocturne, G., and Mariette, X. (2013). Advances in understanding the pathogenesis of primary Sjogren's syndrome. Nat. Rev. Rheumatol. *9*, 544–556. https://doi.org/10.1038/nrrheum.2013.110.
2. Seror, R., Nocturne, G., and Mariette, X. (2021). Current and future therapies for primary Sjogren syndrome. Nat. Rev. Rheumatol. *17*, 475–486. https://doi.org/10.1038/s41584-021-00634-x.
3. Lin, X., Rui, K., Deng, J., Tian, J., Wang, X., Wang, S., Ko, K.H., Jiao, Z., Chan, V.S.F., Lau, C.S., et al. (2015). Th17 cells play a critical role in the development of experimental Sjogren's syndrome. Ann. Rheum. Dis. *74*, 1302–1310. https://doi.org/10.1136/annrheumdis-2013-204584.
4. Fu, W., Liu, X., Lin, X., Feng, H., Sun, L., Li, S., Chen, H., Tang, H., Lu, L., Jin, W., and Dong, C. (2018). Deficiency in T follicular regulatory cells promotes autoimmunity. J. Exp. Med. *215*, 815–825. https://doi.org/10.1084/jem.20170901.
5. Crotty, S. (2014). T follicular helper cell differentiation, function, and roles in disease. Immunity *41*, 529–542. https://doi.org/10.1016/j.immuni.2014.10.004.
6. Craft, J.E. (2012). Follicular helper T cells in immunity and systemic autoimmunity. Nat. Rev. Rheumatol. *8*, 337–347. https://doi.org/10.1038/nrrheum.2012.58.
7. Qi, H. (2016). T follicular helper cells in space-time. Nat. Rev. Immunol. *16*, 612–625. https://doi.org/10.1038/nri.2016.94.
8. Ueno, H., Banchereau, J., and Vinuesa, C.G. (2015). Pathophysiology of T follicular helper cells in humans and mice. Nat. Immunol. *16*, 142–152. https://doi.org/10.1038/ni.3054.
9. Lin, X., Wang, X., Xiao, F., Ma, K., Liu, L., Wang, X., Xu, D., Wang, F., Shi, X., Liu, D., et al. (2019). IL-10-producing regulatory B cells restrain the T follicular helper cell response in primary Sjogren's syndrome. Cell. Mol. Immunol. *16*, 921–931. https://doi.org/10.1038/s41423-019-0227-z.
10. Rothberg, K.G., Heuser, J.E., Donzell, W.C., Ying, Y.S., Glenney, J.R., and Anderson, R.G. (1992). Caveolin, a protein component of caveolae membrane coats. Cell *68*, 673–682. https://doi.org/10.1016/0092-8674(92)90143-z.
11. Razani, B., Combs, T.P., Wang, X.B., Frank, P.G., Park, D.S., Russell, R.G., Li, M., Tang, B., Jelicks, L.A., Scherer, P.E., and Lisanti, M.P. (2002). Caveolin-1-deficient mice are lean, resistant to diet-induced obesity, and show hypertriglyceridemia with adipocyte abnormalities. J. Biol. Chem. *277*, 8635–8647. https://doi.org/10.1074/jbc.M110970200.
12. Wu, H., Deng, R., Chen, X., Wong, W.C., Chen, H., Gao, L., Nie, Y., Wu, W., and Shen, J. (2016). Caveolin-1 Is Critical for Lymphocyte Trafficking into Central Nervous System during Experimental Autoimmune Encephalomyelitis. J. Neurosci. *36*, 5193–5199. https://doi.org/10.1523/JNEUROSCI.3734-15.2016.
13. Medina, F.A., Williams, T.M., Sotgia, F., Tanowitz, H.B., and Lisanti, M.P. (2006). A novel role for caveolin-1 in B lymphocyte function and the development of thymus-independent immune responses. Cell Cycle *5*, 1865–1871. https://doi.org/10.4161/cc.5.16.3132.
14. Minguet, S., Kläsener, K., Schaffer, A.M., Fiala, G.J., Osteso-Ibánez, T., Raute, K., Navarro-Lérida, I., Hartl, F.A., Seidl, M., Reth, M., and Del Pozo, M.A. (2017). Caveolin-1-dependent nanoscale organization of the BCR regulates B cell tolerance. Nat. Immunol. *18*, 1150–1159. https://doi.org/10.1038/ni.3813.
15. Tomassian, T., Humphries, L.A., Liu, S.D., Silva, O., Brooks, D.G., and Miceli, M.C. (2011). Caveolin-1 orchestrates TCR synaptic polarity, signal specificity, and function in CD8 T cells. J. Immunol. *187*, 2993–3002. https://doi.org/10.4049/jimmunol.1101447.
16. Robinson, C.P., Brayer, J., Yamachika, S., Esch, T.R., Peck, A.B., Stewart, C.A., Peen, E., Jonsson, R., and Humphreys-Beher, M.G. (1998). Transfer of human serum IgG to nonobese diabetic Igmu null mice reveals a role for autoantibodies in the loss of secretory function of exocrine tissues in Sjogren's syndrome. Proc. Natl. Acad. Sci. USA *95*, 7538–7543. https://doi.org/10.1073/pnas.95.13.7538.

17. Nwosu, Z.C., Ebert, M.P., Dooley, S., and Meyer, C. (2016). Caveolin-1 in the regulation of cell metabolism: a cancer perspective. Mol. Cancer *15*, 71. https://doi.org/10.1186/s12943-016-0558-7.

18. Zhang, Q., Liu, W., Wang, H., Zhou, H., Bulek, K., Chen, X., Zhang, C.J., Zhao, J., Zhang, R., Liu, C., et al. (2022). TH17 cells promote CNS inflammation by sensing danger signals via Mincle. Nat. Commun. *13*, 2406. https://doi.org/10.1038/s41467-022-30174-1.

19. Lutz, S.E., Smith, J.R., Kim, D.H., Olson, C.V.L., Ellefsen, K., Bates, J.M., Gandhi, S.P., and Agalliu, D. (2017). Caveolin1 Is Required for Th1 Cell Infiltration, but Not Tight Junction Remodeling, at the Blood-Brain Barrier in Autoimmune Neuroinflammation. Cell Rep. *21*, 2104–2117. https://doi.org/10.1016/j.celrep.2017.10.094.

20. Kim, H.J., and Cantor, H. (2011). Regulation of self-tolerance by Qa-1-restricted CD8(+) regulatory T cells. Semin. Immunol. *23*, 446–452. https://doi.org/10.1016/j.smim.2011.06.001.

21. Majumdar, S., Deobagkar-Lele, M., Adiga, V., Raghavan, A., Wadhwa, N., Ahmed, S.M., Rananaware, S.R., Chakraborty, S., Joy, O., and Nandi, D. (2017). Differential susceptibility and maturation of thymocyte subsets during Salmonella Typhimurium infection: insights on the roles of glucocorticoids and Interferon-gamma. Sci. Rep. *7*, 40793. https://doi.org/10.1038/srep40793.

22. Sullivan, B.A., Kraj, P., Weber, D.A., Ignatowicz, L., and Jensen, P.E. (2002). Positive selection of a Qa-1-restricted T cell receptor with specificity for insulin. Immunity *17*, 95–105. https://doi.org/10.1016/s1074-7613(02)00343-6.

23. Wu, M., Yu, S., Yan, S., Wu, M., Zhang, L., Chen, S., Shi, D., Liu, S., Fan, Y., Lin, X., and Shen, J. (2024). Peroxynitrite reduces Treg cell expansion and function by mediating IL-2R nitration and aggravates multiple sclerosis pathogenesis. Redox Biol. *75*, 103240. https://doi.org/10.1016/j.redox.2024.103240.

24. Collins, B.M., Davis, M.J., Hancock, J.F., and Parton, R.G. (2012). Structure-based reassessment of the caveolin signaling model: do caveolae regulate signaling through caveolin-protein interactions? Dev. Cell *23*, 11–20. https://doi.org/10.1016/j.devcel.2012.06.012.

25. Bucci, M., Gratton, J.P., Rudic, R.D., Acevedo, L., Roviezzo, F., Cirino, G., and Sessa, W.C. (2000). In vivo delivery of the caveolin-1 scaffolding domain inhibits nitric oxide synthesis and reduces inflammation. Nat. Med. *6*, 1362–1367. https://doi.org/10.1038/82176.

26. Xu, H., Li, X., Liu, D., Li, J., Zhang, X., Chen, X., Hou, S., Peng, L., Xu, C., Liu, W., et al. (2013). Follicular T-helper cell recruitment governed by bystander B cells and ICOS-driven motility. Nature *496*, 523–527. https://doi.org/10.1038/nature12058.

27. Daynes, R.A., and Jones, D.C. (2002). Emerging roles of PPARs in inflammation and immunity. Nat. Rev. Immunol. *2*, 748–759. https://doi.org/10.1038/nri912.

28. Willson, T.M., Brown, P.J., Sternbach, D.D., and Henke, B.R. (2000). The PPARs: from orphan receptors to drug discovery. J. Med. Chem. *43*, 527–550. https://doi.org/10.1021/jm990554g.

29. Pineda Torra, I., Claudel, T., Duval, C., Kosykh, V., Fruchart, J.C., and Staels, B. (2003). Bile acids induce the expression of the human peroxisome proliferator-activated receptor alpha gene via activation of the farnesoid X receptor. Mol. Endocrinol. *17*, 259–272. https://doi.org/10.1210/me.2002-0120.

30. Popeijus, H.E., van Otterdijk, S.D., van der Krieken, S.E., Konings, M., Serbonij, K., Plat, J., and Mensink, R.P. (2014). Fatty acid chain length and saturation influences PPARalpha transcriptional activation and repression in HepG2 cells. Mol. Nutr. Food Res. *58*, 2342–2349. https://doi.org/10.1002/mnfr.201400314.

31. Chin, J., Hong, J.Y., Lee, J., Hwang, H., Ko, H., Choi, H., Hahn, D., Ko, J., Nam, S.J., Tak, J., et al. (2010). Selective peroxisome proliferator-activated receptor delta isosteric selenium agonists as potent anti-atherogenic agents in vivo. Bioorg. Med. Chem. Lett. *20*, 7239–7242. https://doi.org/10.1016/j.bmcl.2010.10.103.

32. Fernandez-Rojo, M.A., Gongora, M., Fitzsimmons, R.L., Martel, N., Martin, S.D., Nixon, S.J., Brooks, A.J., Ikonomopoulou, M.P., Martin, S., Lo, H.P., et al. (2013). Caveolin-1 is necessary for hepatic oxidative lipid metabolism: evidence for crosstalk between caveolin-1 and bile acid signaling. Cell Rep. *4*, 238–247. https://doi.org/10.1016/j.celrep.2013.06.017.

33. Lim, S.A., Su, W., Chapman, N.M., and Chi, H. (2022). Lipid metabolism in T cell signaling and function. Nat. Chem. Biol. *18*, 470–481. https://doi.org/10.1038/s41589-022-01017-3.

34. Tang, M., Dong, X., Xiao, L., Tan, Z., Luo, X., Yang, L., Li, W., Shi, F., Li, Y., Zhao, L., et al. (2022). CPT1A-mediated fatty acid oxidation promotes cell proliferation via nucleoside metabolism in nasopharyngeal carcinoma. Cell Death Dis. *13*, 331. https://doi.org/10.1038/s41419-022-04730-y.

35. Song, S., Attia, R.R., Connaughton, S., Niesen, M.I., Ness, G.C., Elam, M.B., Hori, R.T., Cook, G.A., and Park, E.A. (2010). Peroxisome proliferator activated receptor alpha (PPARalpha) and PPAR gamma coactivator (PGC-1alpha) induce carnitine palmitoyltransferase IA (CPT-1A) via independent gene elements. Mol. Cell. Endocrinol. *325*, 54–63. https://doi.org/10.1016/j.mce.2010.05.019.

36. A, I.J., Jeannin, E., Wahli, W., and Desvergne, B. (1997). Polarity and specific sequence requirements of peroxisome proliferator-activated receptor (PPAR)/retinoid X receptor heterodimer binding to DNA. A functional analysis of the malic enzyme gene PPAR response element. J. Biol. Chem. *272*, 20108–20117. https://doi.org/10.1074/jbc.272.32.20108.

37. Vunta, H., Davis, F., Palempalli, U.D., Bhat, D., Arner, R.J., Thompson, J.T., Peterson, D.G., Reddy, C.C., and Prabhu, K.S. (2007). The anti-inflammatory effects of selenium are mediated through 15-deoxy-Delta12,14-prostaglandin J2 in macrophages. J. Biol. Chem. *282*, 17964–17973. https://doi.org/10.1074/jbc.M703075200.

38. Chen, H.H., Chen, T.W., and Lin, H. (2009). Prostacyclin-induced peroxisome proliferator-activated receptor-alpha translocation attenuates NF-kappaB and TNF-alpha activation after renal ischemia-reperfusion injury. Am. J. Physiol. Renal Physiol. *297*, F1109–F1118. https://doi.org/10.1152/ajprenal.00057.2009.

39. Mukherjee, R., Jow, L., Croston, G.E., and Paterniti, J.R., Jr. (1997). Identification, characterization, and tissue distribution of human peroxisome proliferator-activated receptor (PPAR) isoforms PPARgamma2 versus PPARgamma1 and activation with retinoid X receptor agonists and antagonists. J. Biol. Chem. *272*, 8071–8076. https://doi.org/10.1074/jbc.272.12.8071.

40. Liu, Y., Guo, G., Zheng, L., Sun, R., Wang, X., Deng, J., Jia, G., Yang, C., Cui, L., Guo, C., et al. (2023). Effectiveness of Fenofibrate in Treatment-Naive Patients With Primary Biliary Cholangitis: A Randomized Clinical Trial. Am. J. Gastroenterol. *118*, 1973–1979. https://doi.org/10.14309/ajg.0000000000002238.

41. Nair, A.B., and Jacob, S. (2016). A simple practice guide for dose conversion between animals and human. J. Basic Clin. Pharm. *7*, 27–31. https://doi.org/10.4103/0976-0105.177703.

42. Selmi, C., Meroni, P.L., and Gershwin, M.E. (2012). Primary biliary cirrhosis and Sjogren's syndrome: autoimmune epithelitis. J. Autoimmun. *39*, 34–42. https://doi.org/10.1016/j.jaut.2011.11.005.

43. Ramos-Casals, M., Brito-Zeron, P., Bombardieri, S., Bootsma, H., De Vita, S., Dorner, T., Fisher, B.A., Gottenberg, J.E., Hernandez-Molina, G., Kocher, A., et al. (2020). EULAR recommendations for the management of Sjogren's syndrome with topical and systemic therapies. Ann. Rheum. Dis. *79*, 3–18. https://doi.org/10.1136/annrheumdis-2019-216114.

44. Glaesener, S., Quách, T.D., Onken, N., Weller-Heinemann, F., Dressler, F., Huppertz, H.I., Thon, A., and Meyer-Bahlburg, A. (2014). Distinct effects of methotrexate and etanercept on the B cell compartment in patients with juvenile idiopathic arthritis. Arthritis Rheumatol. *66*, 2590–2600. https://doi.org/10.1002/art.38736.

45. Young, N.A., Wu, L.C., Bruss, M., Kaffenberger, B.H., Hampton, J., Bolon, B., and Jarjour, W.N. (2015). A chimeric human-mouse model of Sjogren's syndrome. Clin. Immunol. *156*, 1–8. https://doi.org/10.1016/j.clim.2014.10.004.

46. Quinn, J.L., Kumar, G., Agasing, A., Ko, R.M., and Axtell, R.C. (2018). Role of TFH Cells in Promoting T Helper 17-Induced Neuroinflammation. Front. Immunol. *9*, 382. https://doi.org/10.3389/fimmu.2018.00382.

47. Gargalovic, P., and Dory, L. (2003). Caveolins and macrophage lipid metabolism. J. Lipid Res. *44*, 11–21. https://doi.org/10.1194/jlr.r200005-jlr200.

48. Yao, Y., Chen, Z., Zhang, H., Chen, C., Zeng, M., Yunis, J., Wei, Y., Wan, Y., Wang, N., Zhou, M., et al. (2021). Selenium-GPX4 axis protects follicular helper T cells from ferroptosis. Nat. Immunol. *22*, 1127–1139. https://doi.org/10.1038/s41590-021-00996-0.

49. Yang, X.Y., Wang, L.H., Chen, T., Hodge, D.R., Resau, J.H., DaSilva, L., and Farrar, W.L. (2000). Activation of human T lymphocytes is inhibited by peroxisome proliferator-activated receptor gamma (PPARgamma) agonists. PPARgamma co-association with transcription factor NFAT. J. Biol. Chem. *275*, 4541–4544. https://doi.org/10.1074/jbc.275.7.4541.

50. Del Galdo, F., Sotgia, F., de Almeida, C.J., Jasmin, J.F., Musick, M., Lisanti, M.P., and Jiménez, S.A. (2008). Decreased expression of caveolin 1 in patients with systemic sclerosis: crucial role in the pathogenesis of tissue fibrosis. Arthritis Rheum. *58*, 2854–2865. https://doi.org/10.1002/art.23791.

51. Selmi, C., and Gershwin, M.E. (2017). Chronic Autoimmune Epithelitis in Sjögren's Syndrome and Primary Biliary Cholangitis: A Comprehensive Review. Rheumatol. Ther. *4*, 263–279. https://doi.org/10.1007/s40744-017-0074-2.

52. Liu, Y., Wang, J., Luo, S., Zhan, Y., and Lu, Q. (2020). The roles of PPARγ and its agonists in autoimmune diseases: A comprehensive review. J. Autoimmun. *113*, 102510. https://doi.org/10.1016/j.jaut.2020.102510.

53. Ling, H., Luoma, J.T., and Hilleman, D. (2013). A Review of Currently Available Fenofibrate and Fenofibric Acid Formulations. Cardiol. Res. *4*, 47–55. https://doi.org/10.4021/cr270w.

54. Yu, S., Xie, J., Li, P.H., Chen, Y., Tang, I.Y., and Lin, X. (2024). Therapeutic potential of interleukin-17 neutralization in a novel humanized mouse model of Sjögren's disease. Pharmacol. Res. *210*, 107524. https://doi.org/10.1016/j.phrs.2024.107524.

55. Tarn, J.R., Howard-Tripp, N., Lendrem, D.W., Mariette, X., Saraux, A., Devauchelle-Pensec, V., Seror, R., Skelton, A.J., James, K., McMeekin, P., et al. (2019). Symptom-based stratification of patients with primary Sjogren's syndrome: multi-dimensional characterisation of international observational cohorts and reanalyses of randomised clinical trials. Lancet. Rheumatol. *1*, e85–e94. https://doi.org/10.1016/S2665-9913(19)30042-6.

56. Schindelin, J., Arganda-Carreras, I., Frise, E., Kaynig, V., Longair, M., Pietzsch, T., Preibisch, S., Rueden, C., Saalfeld, S., Schmid, B., et al. (2012). Fiji: an open-source platform for biological-image analysis. Nat. Methods *9*, 676–682. https://doi.org/10.1038/nmeth.2019.

57. Bankhead, P., Loughrey, M.B., Fernandez, J.A., Dombrowski, Y., McArt, D. G., Dunne, P.D., McQuaid, S., Gray, R.T., Murray, L.J., Coleman, H.G., et al. (2017). QuPath: Open source software for digital pathology image analysis. Sci. Rep. *7*, 16878. https://doi.org/10.1038/s41598-017-17204-5.

58. Dobin, A., Davis, C.A., Schlesinger, F., Drenkow, J., Zaleski, C., Jha, S., Batut, P., Chaisson, M., and Gingeras, T.R. (2013). STAR: ultrafast universal RNA-seq aligner. Bioinformatics *29*, 15–21. https://doi.org/10.1093/bioinformatics/bts635.

59. Lin, X., Song, J.X., Shaw, P.C., Ng, T.B., Wong, R.N., Sze, S.C., Tong, Y., Lee, K.F., and Zhang, K.Y. (2011). An autoimmunized mouse model recapitulates key features in the pathogenesis of Sjogren's syndrome. Int. Immunol. *23*, 613–624. https://doi.org/10.1093/intimm/dxr066.

60. Fisher, B.A., Jonsson, R., Daniels, T., Bombardieri, M., Brown, R.M., Morgan, P., Bombardieri, S., Ng, W.F., Tzioufas, A.G., Vitali, C., et al. (2017). Standardisation of labial salivary gland histopathology in clinical trials in primary Sjogren's syndrome. Ann. Rheum. Dis. *76*, 1161–1168. https://doi.org/10.1136/annrheumdis-2016-210448.

## STAR★METHODS

### KEY RESOURCES TABLE

| REAGENT or RESOURCE | SOURCE | IDENTIFIER |
|---|---|---|
| Antibodies | | |
| Anti-Aquaporin 5 antibody | Abcam | Cat# ab78486; RRID: AB_1603410 |
| PE Goat anti-mouse IgG (clone Poly4053) | BioLegend | Cat#405307; RRID: AB_315010 |
| APC anti-mouse CD45.2 Antibody (clone 104) | BioLegend | Cat#109814; RRID: AB_389211 |
| FITC anti-mouse CD4 Antibody (clone GK1.5) | BioLegend | Cat#100406; RRID: AB_312691 |
| PE anti-mouse CD4 Antibody (clone GK1.5) | BioLegend | Cat#100408; RRID: AB_312693 |
| PerCP/Cyanine5.5 anti-mouse CD4 (clone GK1.5) | BioLegend | Cat#100434; RRID: AB_893324 |
| APC anti-mouse CD4 Antibody (clone GK1.5) | BioLegend | Cat#100412; RRID: AB_312697 |
| PE anti-human/mouse Bcl-6 Antibody (clone 7D1) | BioLegend | Cat#358504; RRID: AB_2562152 |
| Brilliant Violet 421™ anti-mouse CD19 Antibody (clone 6D5) | BioLegend | Cat#115538; RRID: AB_11203527 |
| APC anti-mouse CD19 Antibody (clone 6D5) | BioLegend | Cat#115512; RRID: AB_313647 |
| Biotin Goat anti-mouse IgG (minimal x-reactivity) Antibody (clone Poly4053) | BioLegend | Cat#405303; RRID: AB_315006 |
| APC anti-mouse/human CD44 (clone IM7) | BioLegend | Cat#103012; RRID: AB_312963 |
| PE/Cyanine7 anti-mouse IL-17A (clone TC11-18H10.1) | BioLegend | Cat#506922; RRID: AB_2125010 |
| PE anti-mouse IL-17A (clone TC11-18H10.1) | BioLegend | Cat#506904; RRID: AB_315464 |
| FITC anti-mouse IFN-γ (clone XMG1.2) | BioLegend | Cat#505806; RRID: AB_315400 |
| Alexa Fluor® 647 anti-mouse FOXP3 (clone MF-14) | BioLegend | Cat#126408; RRID: AB_1089115 |
| Brilliant Violet 421™ anti-mouse CD279 (PD-1) Antibody (clone 29F.1A12) | BioLegend | Cat#135218; RRID: AB_2561447 |
| Brilliant Violet 605™ anti-human/mouse/rat CD278 (ICOS) (clone C398.4A) | BioLegend | Cat#313538; RRID: AB_2687079 |
| PE anti-human/mouse/rat CD278 (ICOS) (clone C398.4A) | BioLegend | Cat#313508; RRID: AB_416332 |
| PE anti-mouse CD185 (CXCR5) (clone L138D7) | BioLegend | Cat#145504; RRID: AB_2561968 |
| Biotin anti-mouse CD185 (CXCR5) (clone L138D7) | BioLegend | Cat#145510; RRID: AB_2562126 |
| APC anti-mouse CD138 (Syndecan-1) Antibody (clone 281-2) | BioLegend | Cat#142506; RRID: AB_10962911 |
| Anti-Mouse IgG (whole molecule) –Alkaline Phosphatase antibody produced in goat | Sigma-Aldrich | Cat#A3562; RRID: AB_258091 |
| PPAR alpha Monoclonal Antibody (3B6/PPAR) | Thermo Fisher Scientific | Cat#MA1-822; RRID: AB_2165745 |
| PPARα Rabbit pAb | ABclonal | Cat#A6697; RRID: AB_2767281 |
| PPARγ Rabbit pAb | ABclonal | Cat# A0270; RRID: AB_2757083 |
| Caveolin-1 (D46G3) XP® Rabbit mAb | Cell Signaling Technology | Cat#3267; RRID: AB_2275453 |
| β-Actin (8H10D10) Mouse | Cell Signaling Technology | Cat#3700; RRID: AB_2242334 |
| PFKFB3 (D7H4Q) Rabbit mAb | Cell Signaling Technology | Cat#13123; RRID: AB_2617178 |
| Phospho-PFK-2 (Ser466) Antibody | Cell Signaling Technology | Cat#4081 |
| SDHA (D6J9M) XP® Rabbit mAb | Cell Signaling Technology | Cat#11998; RRID: AB_2750900 |
| ACO2 (D6D9) XP® Rabbit mAb | Cell Signaling Technology | Cat#6571; RRID: AB_2797630 |
| ACADM Rabbit pAb | ABclonal | Cat#A1873; RRID: AB_2763906 |
| Anti-F-actin antibody [NH3] | Abcam | Cat#ab205; RRID: AB_302794 |
| APC anti-mouse/human CD45R/B220 Antibody (clone RA3-6B2) | BioLegend | Cat#103212; RRID: AB_312997 |
| FITC anti-mouse/human GL7 (clone GL7) | BioLegend | Cat#144603; RRID: AB_2561696 |
| PE anti-mouse CD95 (Fas) (clone SA367H8) | BioLegend | Cat#152608; RRID: AB_2632902 |

(*Continued on next page*)

*Continued*

| REAGENT or RESOURCE | SOURCE | IDENTIFIER |
|---|---|---|
| PE anti-mouse CD154 Antibody (clone MR1) | BioLegend | Cat#106506; RRID: AB_313271 |
| Ultra-LEAF™ Purified anti-human/mouse/rat CD278 (ICOS) Antibody (clone C398.4A) | BioLegend | Cat#313540; RRID: AB_2687114 |
| Anti-ATPB antibody [3D5] - Mitochondrial Marker | Abcam | Cat#ab14730; RRID: AB_301438 |
| APC anti-mouse CD36 Antibody (clone HM36) | BioLegend | Cat#102612; RRID: AB_2072639 |
| PerCP/Cyanine5.5 anti-human CD4 (clone OKT4) | BioLegend | Cat#317428; RRID: AB_1186122 |
| Biotin anti-human CD185 (CXCR5) (clone J252D4) | BioLegend | Cat#356932; RRID: AB_2566499 |
| PE/Cyanine7 anti-human CD279 (PD-1) (clone A17188B) | BioLegend | Cat#621616; RRID: AB_2832836 |
| PE Streptavidin | BioLegend | Cat#405203 |
| PE/Cyanine7 Streptavidin | BioLegend | Cat#405206 |
| Goat anti-Rabbit IgG (H + L) Cross-Adsorbed Secondary Antibody, Alexa Fluor™ 488 | Thermo Fisher Scientific | Cat#A-11008; RRID: AB_143165 |
| Goat anti-Mouse IgG (H + L) Cross-Adsorbed Secondary Antibody, Alexa Fluor™ 488 | Thermo Fisher Scientific | Cat#A-11001; RRID: AB_2534069 |
| Goat anti-Rabbit IgG (H + L) Cross-Adsorbed Secondary Antibody, Alexa Fluor™ 568 | Thermo Fisher Scientific | Cat#A-11011; RRID: AB_143157 |
| Goat anti-Mouse IgG (H + L) Cross-Adsorbed Secondary Antibody, Alexa Fluor™ 568 | Thermo Fisher Scientific | Cat#A-11004; RRID: AB_2534072 |
| Ultra-LEAF™ Purified anti-mouse CD28 Antibody (clone 37.51) | BioLegend | Cat#102116; RRID: AB_11147170 |
| Ultra-LEAF™ Purified anti-mouse CD3 Antibody (clone 17A2) | BioLegend | Cat#100238; RRID: AB_2561487 |
| Ultra-LEAF™ Purified anti-human CD28 Antibody (clone CD28.2) | BioLegend | Cat#302934; RRID: AB_11148949 |
| Ultra-LEAF™ Purified anti-human CD3 Antibody (clone UCHT1) | BioLegend | Cat#300438; RRID: AB_11146991 |
| Ultra-LEAF™ Purified anti-mouse IFN-γ Antibody (clone R4-6A2) | BioLegend | Cat#505709; RRID: AB_2832805 |
| Ultra-LEAF™ Purified anti-mouse IL-4 Antibody (clone 11B11) | BioLegend | Cat#504122; RRID: AB_11150601 |
| Ultra-LEAF™ Purified anti-human/mouse TGF-β1 Recombinant Antibody (clone QA18A10) | BioLegend | Cat#947304; RRID: AB_2910510 |
| Ultra-LEAF™ Purified anti-human IFN-γ Antibody (clone B27) | BioLegend | Cat#506532; RRID: AB_2801092 |
| Ultra-LEAF™ Purified anti-human IL-4 Recombinant Antibody (clone QA20A30) | BioLegend | Cat#945304; RRID: AB_2892511 |
| Anti-BrdU antibody [BU1/75 (ICR1)] - Proliferation Marker | Abcam | Cat#ab6326; RRID: AB_305426 |
| Recombinant Mouse CXCL13 (carrier-free) | BioLegend | Cat#583908 |
| Recombinant Human CXCL13 (carrier-free) | BioLegend | Cat#574706 |
| **Biological samples** | | |
| Plasma samples from healthy donors | Hong Kong Red Cross | N/A |
| Plasma samples from SjD patients | Queen Mary Hospital and Peking University Third Hospital | N/A |
| **Chemicals, peptides, and recombinant proteins** | | |
| DAPI | Molecular Probes | Cat#D1306 |
| $M3R^{2ND}$ | SBS Genetech | Sequence: QYFVGKRTVPPGECFIQFLSEP |
| $SSA/Ro60^{274-290}$ | SBS Genetech | Sequence: QEMPLTALLRNLGKMT |
| Pilocarpine Hydrochloride | Sigma-Aldrich | Cat#PHR1493; CAS: 54-71-7 |
| Phorbol 12-myristate 13-acetate | Sigma-Aldrich | Cat#P8139; CAS: 16561-29-8 |

(*Continued on next page*)

*Continued*

| REAGENT or RESOURCE | SOURCE | IDENTIFIER |
|---|---|---|
| Ionomycin from Streptomyces conglobatus | Sigma-Aldrich | Cat#I9657; CAS: 56092-81-0 |
| Monensin Solution (1,000X) | BioLegend | Cat#420701 |
| SIGMAFAST™ BCIP®/NBT | Sigma-Aldrich | Cat#B5655 |
| Cavtratin | Enzo Life Sciences | Cat#ALX-153-064-M005; Sequence: RQIKIWFQNRRMKWKKDGIW KASFTTFTVTKYWFYR |
| Recombinant Mouse B7-H2 (ICOSL)-Fc Chimera (carrier-free) | BioLegend | Cat#792706 |
| Recombinant Mouse IL-21 (carrier-free) | BioLegend | Cat#574508 |
| Recombinant Mouse IL-6 (carrier-free) | BioLegend | Cat#575708 |
| RPMI 1640 Medium | Gibco | Cat#11875093 |
| X-VIVO™ 20 Serum-free Hematopoietic Cell Medium | Lonza | Cat#BE04-448Q |
| Bovine Serum Albumin | Sigma-Aldrich | Cat#A8806 |
| PBS (10X), pH 7.4 | Gibco | Cat#70011044 |
| Fetal Bovine Serum (FBS) | Gibco | Cat#10270106 |
| Penicillin-Streptomycin (10,000 U/mL) | Gibco | Cat#15140122 |
| ACK Lysing Buffer | Gibco | Cat#A1049201 |
| RNAiso Plus (Total RNA extraction reagent) | TaKaRa | Cat#9109; CAS: 9048-46-8 |
| Iso-Propyl Alcohol | Duksan reagents | Cat#3375; CAS: 67-63-0 |
| Ethanol absolute | VWR Chemicals | Cat#20821.330; CAS: 64-17-5 |
| DEPC-Treated Water | Thermo Fisher Scientific | Cat#AM9922 |
| Chloroform | Duksan reagents | Cat#6938; CAS: 67-66-3 |
| GW6471 | TargetMol | Cat#T8486; CAS: 880635-03-0 |
| 15-deoxy-Δ12,14-Prostaglandin J2 | Cayman Chemical | Cat#18570; CAS: 87893-55-8 |
| (±)8-HEPE | Cayman Chemical | Cat#32340; CAS: 99217-77-3 |
| GSK3787 | TargetMol | Cat#T1941; CAS: 188591-46-0 |
| Dimethyl sulfoxide | Sigma-Aldrich | Cat#D8418; CAS: 67-68-5 |
| Fenofibrate | MedChemExpress | Cat#HY-17356; CAS: 49562-28-9 |
| 2-NBDG (2-(N-(7-Nitrobenz-2-oxa-1,3-diazol-4-yl) Amino)-2-Deoxyglucose) | Thermo Fisher Scientific | Cat#N13195 |
| BODIPY™ FL C16 (4,4-Difluoro-5,7-Dimethyl-4-Bora-3a,4a-Diaza-*s*-Indacene-3-Hexadecanoic Acid) | Thermo Fisher Scientific | Cat#D3821 |
| Glucose Solution | Gibco | Cat#A2494001 |
| Oligomycin, ATP synthase inhibitor | Abcam | Cat#ab141904; CAS: 1397-94-0 |
| FCCP, mitochondrial oxidative phosphorylation uncoupler | Abcam | Cat#ab120081; CAS: 370-86-5 |
| Rotenone, mitochondrial electron transport chain inhibitor | Abcam | Cat#ab143145; CAS: 83-79-4 |
| Antimycin A, Antibiotic | Abcam | Cat#ab141829; CAS: 1404-19-9 |
| Palmitic acid | TargetMol | Cat#T2908; CAS: 57-10-3 |
| Etomoxir sodium salt | TargetMol | Cat#T4535; CAS: 828934-41-4 |
| Seahorse XFp Media & Calibrant | Agilent | Cat#100840-000 |
| Seahorse XF DMEM Medium | Agilent | Cat#103575-503 |
| GW7647 | TargetMol | Cat#T15453; CAS: 265129-71-3 |
| Pioglitazone hydrochloride | TargetMol | Cat#T0214L; CAS: 112529-15-4 |
| SC-560 | TargetMol | Cat#T4101; CAS: 188817-13-2 |
| Lymphoprep™ | STEMCELL Technologies | Cat#07801 |
| Tissue Freezing Medium | Leica Biosystems | Cat#14020108926 |

(*Continued on next page*)

*Continued*

| REAGENT or RESOURCE | SOURCE | IDENTIFIER |
|---|---|---|
| Freund's Adjuvant, Incomplete | Sigma-Aldrich | Cat#F5506 |
| Freund's Adjuvant, Complete | Sigma-Aldrich | Cat#F5881 |
| Fluorescence Mounting Medium | Dako Omnis | Cat#S3023 |
| UltraPure™ Low Melting Point Agarose | Thermo Fisher Scientific | Cat#16520-050 |
| **Critical commercial assays** | | |
| *In Situ* Cell Death Detection Kit | Roche | Cat#11684795910 |
| Zombie Aqua™ Fixable Viability Kit | BioLegend | Cat#423102 |
| Foxp3 transcription factor staining buffer set | eBioscience | Cat#00-5521-00 |
| Fixation/Permeabilization Kit | BD Biosciences | Cat#554714 |
| CellTracker™ Orange CMTMR Dye | Thermo Fisher Scientific | Cat#C2927 |
| CFSE Cell Division Tracker Kit | BioLegend | Cat#423801 |
| LEGEND MAX™ Mouse IFN-γ ELISA Kit | BioLegend | Cat#430807 |
| LEGEND MAX™ Mouse TNF-α ELISA Kit | BioLegend | Cat#430907 |
| LEGEND MAX™ Mouse IL-17A ELISA Kit | BioLegend | Cat#432507 |
| Mouse IL-21 DuoSet ELISA | R&D Systems | Cat#DY594 |
| ChIP Assay Kit | Beyotime | Cat#P2078 |
| PrimeScript™ RT Reagent Kit with gDNA Eraser (Perfect Real Time) | TaKaRa | Cat#RR047A |
| TB Green® Premix Ex Taq™ II (Tli RNase H Plus) | TaKaRa | Cat#RR820A |
| Free Fatty Acid Fluorometric Assay Kit | Cayman Chemical | Cat#700310 |
| P3 Primary Cell 4D-Nucleofector® X Kit L | Lonza | Cat#V4XP-3024 |
| CD4 (L3T4) MicroBeads, mouse | Miltenyi Biotec | Cat#130-117-043 |
| CD4 MicroBeads, human | Miltenyi Biotec | Cat#130-045-101 |
| H&E Staining Kit | Abcam | Cat#ab245880 |
| Pierce™ ECL Western Blotting Substrate | Thermo Fisher Scientific | Cat#32109 |
| Promoter-Binding TF Profiling Plate Array II | Signosis | Cat#FA-2002 |
| Nuclear Extraction Kit | Signosis | Cat#SK-0001 |
| **Deposited data** | | |
| RNA-Seq | This Paper | Database: HRA005595 |
| **Experimental models: Organisms/strains** | | |
| Cav1−/− mice (STOCK Cav1tm1Mls/J) | The Jackson Laboratory | JAX:004585 |
| NOD.Cg-PrkdcscidIl2rgtm1Wjl/SzJ (NSG) mice | CCMR, HKU | N/A |
| C57BL/6N | CCMR, HKU | N/A |
| **Oligonucleotides** | | |
| Primers see Table S1 | Integrated DNA Technologies | N/A |
| **Recombinant DNA** | | |
| Plasmid: GFP-homo-caveolin 1 | Guangzhou IGE Biotechnology | NCBI Reference Sequence: NM_001172895.1 |
| Plasmid: GFP-mus musculus-PPARα | Guangzhou IGE Biotechnology | NCBI Reference Sequence: NM_011144.6 |
| Plasmid: mcherry- mus musculus-CPT1a | Guangzhou IGE Biotechnology | NCBI Reference Sequence: NM_013495.2 |
| **Software and algorithms** | | |
| FlowJo (v10.2) | BD Biosciences | https://www.flowjo.com |
| Prism (v8.4.0) | GraphPad Software Inc | https://www.graphpad.com/ |
| Fiji-ImageJ | Schneider et al.[56] | https://imagej.nih.gov/ij/ |
| QuPath (v0.3.2) | Bankhead et al.[57] | https://qupath.github.io |
| ZEN Microscopy Software | Zeiss version 2.3 | https://www.zeiss.com/microscopy/en/products/software/zeiss-zen.html |
| STAR (v2.6.1) | Dobin et al.[58] | http://code.google.com/p/rna-star/ |
| R (v3.6.1) | The R Foundation | https://www.r-project.org |

(*Continued on next page*)

*Continued*

| REAGENT or RESOURCE | SOURCE | IDENTIFIER |
|---|---|---|
| MetaMorph (7.8.0.0) | Molecular Devices | http://www.moleculardevices.com/products/software/meta-imaging-series/metamorph.html |
| IMARIS (v10.0.0) | Oxford Instruments | https://imaris.oxinst.com/ |

## EXPERIMENTAL MODEL AND STUDY PARTICIPANT DETAILS

### Human samples and ethics

A total of 24 SjD patients (all females) were recruited from Queen Mary Hospital, Hong Kong and Peking University Third Hospital, Peking, China. SjD diagnosis was based on the 2002 American-European Consensus Group classification criteria. Subjects overlapping with any other autoimmune diseases or not fulfilling the diagnostic criteria were excluded. Informed consent was obtained from all patients. Ethics approval was obtained from the Institutional Review Board of Queen Mary Hospital, the University of Hong Kong (IRB UW 20–579; IRB UW 21–167), and the Medical Ethical Committee of Peking University Third Hospital, Peking, China (IRB00006761-M2020456).

### Mice and ethics

Female mice of C57BL/6N background (6-8-week old) and female *NOD.Cg-Prkdcscidll2rgtm1Wjl/SzJ* (NSG) mice (4-6-week old) were obtained from the Center for Comparative Medicine Research (CCMR), the University of Hong Kong. Caveolin-1 knock-out (Cav1−/−) mice were purchased from The Jackson Laboratory. All mouse strains were maintained under an AAALAC International accredited program at the Center for Comparative Medicine Research, HKU under Specific Pathogen Free (SPF) conditions and performed following the approved national and institutional regulations and guidelines (Ref. No. 5448-20; 5069-19; 5607-21; 5622-21).

### ESS induction in mice

Female C57BL/6N mice in 6-week-old were immunized to induce the experimental SS (ESS) model as we previously described.[3] In brief, proteins extracted from the bilateral salivary glands (SG) of normal mice were emulsified in an equal volume of Freund's complete adjuvant at a final concentration of 2 mg/mL. For ESS induction, on day 0, each mouse received subcutaneous injections on the back with 0.2 mL of the emulsion. On day 14, a booster injection was conducted with a final concentration of 1 mg/mL SG proteins emulsified in an equal volume of Freund's incomplete adjuvant. Female NSG mice were immunized in the identical manner. The ESS mice were compared between wild type (WT) and Cav1−/− mice. Each group included 6–8 female mice.

### Primary murine naive CD4$^+$ T cell culture

Murine naive CD4$^+$ T cells were purified by mouse CD4 MicroBeads from total lymphocytes and splenocytes obtained from female C57BL/6 mice via magnetic activated cell sorting (MACS), following the manufacturer instructions. Then enriched cells were washed with PBS buffer and resuspended in RPMI 1640 medium supplemented with 10% fetal bovine serum (FBS), and 1% penicillin-streptomycin. CD4$^+$ T cells were cultured at $1\times10^6$ per mL in a 24-well cell culture plate precoated with anti-CD3 and anti-CD28 antibodies (1 μg/mL). For Tfh differentiation, recombinant murine IL-6 (25 ng/mL) and IL-21 (10 ng/mL) and 5 μg/mL of anti-IFN-γ, anti-IL-4 and anti-TGF-β neutralizing antibodies were added. After 3 days of incubation at 37°C and 5% $CO_2$, the cells were washed and pelleted for further use or analysis.

### Primary human naive CD4$^+$ T cell culture

Peripheral blood mononuclear cells (PBMCs) were isolated by Lymphoprep density gradient medium, following the manufacturer instructions. Then human naive CD4$^+$ T cells were purified by human CD4 MicroBeads from PBMCs, and recombinant human IL-6 (25 ng/mL) and IL-21 (10 ng/mL) and 5 μg/mL of anti-IFN-γ, anti-IL-4 and anti-TGF-β neutralizing antibodies were added for Tfh differentiation.

## METHOD DETAILS

### Construction of bone marrow chimaeras

Both donor and recipient mice were female in all experiments. The recipient mice will receive sub-lethal irradiation (680 cGy) to remove hematopoietic cells. Bone marrow cells will be prepared from donor mice and suspended in PBS to obtain a final concentration of $1x10^7$ cells/300 μL. Each recipient mice will receive intravenous injection of bone marrow cells from wild type (WT) or Cav1−/− mice via tail vein at 8 h after irradiation. The mice will be provided with enrofloxacin (5mg/kg) for 2 weeks. The experiment was performed with chimaeras 10 weeks after the initial reconstitution.

### Human cell collection

PBMCs from SjD patients or healthy donors were isolated by Lymphoprep density gradient medium, following the manufacturer instructions. The correlation exists between Cav-1 and PPARα or ICOS was calculated by Pearson's correlation coefficient.

### Saliva and blood collection

To induce saliva secretion, mice were anesthetised, followed by intraperitoneal injection of pilocarpine (5 mg/kg body weight, Sigma-Aldrich).[59] Stimulated saliva was gravimetrically collected using a 20 μL sized pipet tip from the oral cavity for 15 min.

Blood samples were collected and incubated at room temperature (RT) for 30 min. Samples were centrifuged at 1,500×g for 10 min for serum separation.

### Histological assessment

Murine organs, i.e., salivary glands, were frozen in optimal cutting temperature compound (OCT) for sectioning (10 μm), then fixed and followed by haematoxylin and eosin (H&E) staining. The sections were imaged under NanoZoomer at 10× magnification. The injured areas were analyzed using Fiji and ZEN Microscopy Software. In brief, negative infiltration refers to score 0, positive infiltration but less than 50 lymphocytes per 4mm$^2$ refers to score 1, positive infiltration with more than 50 lymphocytes per 4mm$^2$ refers to score 2, while ectopic lymphoid structure detection refers to score 3, assessed by positive staining of CD3, B220 and CD21, in accordance with EULAR consensus guidelines.[60]

### Immunofluorescence microscopy

Mouse spleen and lymph node tissues were frozen in OCT for sectioning (10 μm), and fixed in 4% paraformaldehyde (PFA) solution. Then the sections were washed with PBS and blocked in protein blocking agent (PBA) buffer at RT for 1 h. After that, the sections were incubated with fluorochrome-labeled anti-mouse antibodies overnight at 4°C or incubated with primary anti-mouse antibodies overnight at 4°C followed by incubating with a fluorochrome-labeled secondary antibody at RT for 1 h. Then washed the slices with PBS and nuclei were counterstained with DAPI at RT for 5 min. The slices were mounted with fluorescence mounting medium and scanned with a Zeiss LSM 880 using ×20 air or ×40 oil immersion lens.

To examine the autoantibodies deposition on the salivary epithelium, the tissue sections were stained with AQP-5 and monoclonal antibodies against mouse IgG. A rat IgG antibody was used for control staining. The tissue sections were also incubated with a rabbit anti-mouse AQP-5 antibody followed by a goat anti-rabbit IgG-FITC antibody. The MFI of salivary-deposited IgG per acinus was quantified by Fiji and normalized to the MFI of isotype IgG staining.

To determine the CD4$^+$ T cell homing to B cell follicles, non-consecutive sections were used to avoid the same follicle and its associated T-B border being repeatedly counted. Staining reagents included FITC anti-CD4, PE anti-ICOS, APC anti-B220. The homing coefficient was calculated as previously described.[26] In brief, T cells were quantified in the B cell zone (follicles) and T-B borders, and the homing coefficient equals the ratio of the T cell densities of these two regions, as Homing coefficient = T cell density in the follicles/T cell density in the T-B borders.

### Two-photon live imaging of T/B cells motility *in vivo*

To visualize WT or Cav1−/− T cells and B cells motility *in vivo*, CD4$^+$ T cells from WT or Cav1−/− ESS mice were purified and labeled with CFSE Cell Division Tracker Kit (CFSE) and WT B cells were purified and labeled with CellTracker Orange CMTMR Dye (CMTMR) following the manufacturer instructions before being adoptively transferred into NSG mice. After 3 days, the spleen from NSG mice was carefully imaged by motorized Olympus FVMPE-RS Hybrid Multiphoton System, which was composed of a Coherent Chameleon Vision II laser and an Olympus FVMPE-RS motorized upright microscope equipped with a water immersion lens (×25, NA 1.05, Olympus). The motorized stage on which live mice were imaged was enclosed in a customized heating pad maintained at 37°C. To capture T cell migration at T-B borders and follicles in three dimensions, z stack imaging (30 μm depth with 1 μm per step) was conducted at a time resolution of 20s per frame. Each imaging sequence was 30 min in duration. After acquisition, four-dimensional datasets were analyzed using Imaris software (Bitplane, version 10.0) with Surface and cell-tracking modules. Cell tracks that lasted for less than 2 min were excluded from the analysis.

### Transwell migration assay

T cells were cultured 3 days for Tfh differentiation before being loaded as a 500 μL suspension of 10$^6$ cells into the upper transwell in a 24-well-plate format (5 μm pore, Corning). The cell suspension was supplemented with the anti-ICOS or isotype-matched control antibody at a final concentration of 10 μg/mL. Recombinant CXCL13 of 1 μg/mL concentrations was added to the bottom wells before the cells were allowed to *trans*-migrate for 6 h at 37°C in an incubator. Cells that on the upper wells and have migrated to the bottom wells were analyzed by flow cytometry.

### Imaging of T cell actin cytoskeleton *in vitro*

T cells were cultured 3 days for Tfh differentiation before being incubated with 5 μg/mL isotype control or anti-ICOS antibody at 37°C for 1 h. Then dropped onto poly-L-lysine- coated glass (Electron Microscopy Science) for incubation at 37°C for 30 min. Fixed with

4% paraformaldehyde and stained for F-actin with Alexa Fluor 488 Conjugate, APC anti-CD4 and DAPI. The slices were mounted with fluorescence mounting medium and scanned with a Zeiss LSM 880 using ×63 oil immersion lens.

### Imaging of T cell motility *in vitro*

T cells extracted from WT or Cav1−/− mice were cultured 3 days for Tfh differentiation. Then stained the cells with Zombie Aqua Fixable Viability Kit to separate live and died cells following stained by BV421 anti-PD1 and APC anti-CD4 for 30 min at 4°C in cell culture medium. Tfh cells ($PD1^+CD4^+$) were sorted by the BD FACSAriaTM Fusion Cell Sorter. 20,000 Tfh cells were seeded into 48-well plate incubated with 5 μg/mL isotype control or anti-ICOS antibody at 37°C for 30 min. The cell trajectory was monitored by Nikon Ti2-E for 10 min. Images were acquired at one frame per five seconds. Data was acquired by Metamorph software, and processed by ImageJ and Imaris.

### Flow cytometry

Single cell suspensions were extracted from mouse spleen and lymph nodes. Zombie Aqua Fixable Viability Kit was firstly stained to separate the live and died cells. Then incubated with Fc-blocking (CD16/32) antibody for 10 min at 4°C prior to staining with fluorochrome-conjugated antibodies overnight at 4°C. Single cell suspensions were cultured in RPMI 1640 medium containing 10% FBS with PMA (50 ng/mL), ionomycin (500 ng/mL) and monensin for 4 h before performing intracellular staining for cytokines as IL-10, IFNγ and IL-17 by the BD Fixation/Permeabilization Solution Kit. Intranuclear staining was performed with anti-FoxP3 and anti-Blimp-1 antibodies using a FoxP3-staining buffer following the protocols of the manufacturer. Stained cells were analyzed with a FACS Fortessa flow cytometer (BD Biosciences), and acquired data were analyzed with FlowJo software.

### Western blot analysis

$CD4^+$ T cells were purified from total lymphocytes and splenocytes isolated from different stages of ESS C57BL/6 mice. Then Cell pellets were lysed with RIPA buffer supplemented with proteinase inhibitors and phosphatase inhibitors. Protein samples were loaded on 12% SDS-PAGE and transferred onto the PVDF membrane. The membrane was blocked with 5% BSA in TBST and then incubated with anti-Caveolin 1, PPARα or metabolism related primary antibodies at 4°C overnight and incubated with secondary antibody at RT for 2 h. The immunoreactivities were detected by ECL Western Blotting Substrate and captured by a chemiluminescence imaging system (Bio-Rad).

### ELISA

For autoantibody detection, peptides with sequences of the second extracellular loop of the murine M3 muscarinic receptor ($M3R^{2nd}$, QYFVGKRTVPPGECFIQFLSEP) and SSA/$Ro60^{274-290}$ (QEMPLTALLRNLGKMT) were synthesized. Antibodies and cytokines in serum and cellular supernatant were determined by ELISA kits as previously described[3] following the manufacturer instructions.

### ELISpot assay

Live cells were seeded in the MultiScreen HTS plates (Millipore) which were pre-coated with SSA/$Ro60^{274-290}$ peptides overnight. Sorting-purified B cells were stimulated with LPS (2 μg/mL) for 48 h followed by addition of alkaline phosphatase-conjugated anti-mouse IgG antibodies. Spots were developed by using BCIP/NBT Chromogenic Kit and visualized by ImmunoSpot Analyzer (Cellular Technology Limited).

### RT-qPCR and RNA-seq analysis

Total RNA was extracted from cells by RNAiso Plus. cDNA was reverse transcripted by PrimeScriptTM RT reagent Kit. RT-qPCR was performed using SYBR Green Mix with LC480 (Roche). All the procedures were performed following the manufacturer's instructions. The relative mRNA levels, normalized to the expression of 18s, were calculated by the ΔΔCt method. RNA preparation, library construction and sequencing on BGISEQ-500 were performed at the Beijing Genomics Institute (BGI). Gene expression levels were quantified by the software package RSEM. DESeq2 and Poisson distribution method were used to screen differentially expressed genes. Heatmaps were generated using Microsoft Excel. GO and KEGG database were used to extrapolate differentially expressed pathways. The RNA-seq data in this study were available upon request.

### Chromatin immunoprecipitation (ChIP)-qPCR

ChIP was performed by the following protocol of the ChIP Assay Kit. In brief, each one 10 cm-dish of T cells ($1\times10^7$) was treated with GW6471 or vehicle respectively for 30 min, and induced the cells into Tfh differentiation for 12 h. Then cross-linked the cells with 1% formaldehyde and proceeded to washing steps with cold PBS. Harvested the cells and subjected to cellular and nuclear lysis. The whole nuclear lysate was sheared by a sonicator with optimal condition (10s pulse on, 20 s pulse off, 20 cycles, 40% amplitude) to yield 200–800bp DNA. 20 μL of sheared lysate was aliquoted as Input. The left 2 mL of the sheared lysate was subjected to immunoprecipitation by overnight incubation of either anti-PPARα antibody or IgG control. The immunoprecipitated DNA and input DNA were purified and amplified by quantitative RT-PCR.

### Seahorse assay

For oxygen consumption rate (OCR) analysis, $10^6$ cells per well were seeded in the appropriate cell culture growth medium in 24-well plates designed for the Seahorse XFe24 Analyzer (Agilent). For glucose assay, the Seahorse XF DMEM was composed with 1 mM pyruvate and 10 mM glucose, and for fatty acid assay, the Seahorse XF DMEM should be composed with 200 μM palmitic acid as the sole substrate. A program with a typical 8-min cycle of mix (3 min), dwell (2 min), and measurement (3 min) was used using an XF24 Extracellular Flux Analyzer (Seahorse Bioscience). During measurement, oligomycin, FCCP and Rotenone+antimycin A were added to a final concentration of 10 μM, 20 μM and 10μM + 1 μM, respectively.

### Transcription factor (TF) binding profiling

The active TFs were evaluated by the Promoter Binding TF Profiling Plate Array II Kit following manufacturer instructions. Briefly, $CD4^+$ T cells were isolated from naive WT or $Cav1^{-/-}$ mice and cultured under Tfh polarization conditions. After 16h, the nuclear extracts were prepared by Nuclear Extraction Kit following manufacturer instructions, while 10 μg nuclear extracts were incubated with TF binding oligo probe mix. Then probed TF DNA complex was eluted and hybridized in the plate before measurement in the luminometer plate reader. Wilms tumor suppressor protein 1 (WT1) was used as the blank control to normalize the readings.

## QUANTIFICATION AND STATISTICAL ANALYSIS

### Polarized states of Tfh cells

For quantitative analysis of polarized states of Tfh cells according to the F-actin staining. The shape index (SI) was calculated as following: SI = cell length divided by its width at the middle along the length. If SI is no less than 2 or the cell display at least one pseudopod protrusion when SI is less than 2, the cell is considered polarized.

### Quantification of cell migration

Cell migration imaged by Nikon Ti2-E was analyzed by Metamorph software with manual supervision and verification. Cell tracks that lasted for less than 2 min were excluded from analysis. Analysis of mean squared displacements included data for 10 min. The centroid velocity and directional persistence were measured as displacement -normalized path length.

### Statistical analysis

Statistical analysis was performed by using the GraphPad Prism. The data were assessed with unpaired Mann Whitney test to compare two groups, one-way ANOVA Kruskal-Wallis with Dunn's multiple comparisons test or two-way ANOVA to compare multiple groups and Pearson's correlation coefficient to analyze the correlation between two parameters as stated in the figure legends. $p < 0.05$ was considered statistically significant.